Laser Beacon Tracking for Free-space Optical Communication on Small-Satellite Platforms in Low-Earth Orbit

by

Tam Nguyen Thuc Nguyen

S.B., Massachusetts Institute of Technology (2013)

Submitted to the Department of Aeronautics and Astronautics
in partial fulfillment of the requirements for the degree of

Master of Science in Aeronautics and Astronautics

at the

MASSACHUSETTS INSTITUTE OF TECHNOLOGY

September 2015

Author . . . .
Department of Aeronautics and Astronautics
August 20, 2015

Certified by. . . . .
Kerri Cahoy
Assistant Professor of Aeronautics and Astronautics
Thesis Supervisor

Accepted by . . . .
Paulo Lozano
Chairman, Department Committee on Graduate Theses

Laser Beacon Tracking for Free-space Optical Communication on Small-Satellite Platforms in Low-Earth Orbit

by

Tam Nguyen Thuc Nguyen

Submitted to the Department of Aeronautics and Astronautics
on August 20, 2015, in partial fulfillment of the
requirements for the degree of
Master of Science in Aeronautics and Astronautics

Abstract

Free-space optical (FSO) communication, or laser communication, is capable of providing high-rate communication links, meeting the growing downlink demand of space missions, including those on small-satellite platforms. FSO communication takes advantage of the high-gain nature of narrow laser beams to achieve higher link efficiency than traditional radio-frequency systems. In order for a FSO link to be established and maintained, the spacecraft's attitude determination and control system needs to provide accurate pointing at the optical ground station. However, small satellites, such as CubeSats, have limited ground-tracking capabilities with existing attitude sensors. Miniaturized laser beacon tracking system, on the other hand, has the potential to provide precise ground-based attitude knowledge, enabling laser communication to be accomplished on small-satellite platforms. This thesis details the development of a CubeSat-sized laser beacon camera capable of achieving a sub-milliradian attitude knowledge accuracy with low fade probability during various sky conditions, sufficient to support a high-rate FSO communication link on a CubeSat platform on low-Earth orbit. The high-level Nanosatellite Optical Downlink Experiment (NODE) system architecture, the beacon camera conceptual design as well as prototype development are presented in detail. An end-to-end beacon simulation was constructed to validate the attitude sensing performance of the module under expected atmospheric turbulence and sky brightness conditions. The simulation results show a high-accuracy attitude sensing performance and low fade probability, capable of supporting NODE's laser links.

Thesis Supervisor: Kerri Cahoy
Title: Assistant Professor of Aeronautics and Astronautics

Acknowledgments

THIS PAGE INTENTIONALLY LEFT BLANK

Contents

List of Figures

9

THIS PAGE INTENTIONALLY LEFT BLANK

List of Tables

THIS PAGE INTENTIONALLY LEFT BLANK

Nomenclature

ω_s slew rate

σ_i^2 scintillation index

A_R receive aperture area

C_n^2 refractive index structure parameter

d ground-to-satellite range

k beacon wavenumber

L_A atmospheric loss

L_O optics loss

P_R transmit power

P_T received power

S/N_b signal-to-brightest-noise ratio

V_G ground wind speed

w RMS wind speed

ADCS   attitude determination and control system

BPFF   brightest pixel flux fraction

CCD   charge-coupled device

CMOS complementary metal-oxide semiconductor

COM center-of-mass

COTS commercial off-the-shelf

DN   image pixel digital number

EDFA Erbium Doped Fiber Amplfier

EIRP equivalent isotropic radiated power

FFT   Fast Fourier Transform

FOV   field-of-view

FRAM Flight Releasable Attachment Mechanism

FSM   fast-steering mirror

GPS   Global Positioning System

ISS   International Space Station

LADEE Lunar Atmospheric and Dust Environment Explorer

LEO   low-Earth orbit

LLCD Laser Lunar Communication Demonstration

LLCS Laser Lunar Communication System

LSB   least-significant bit

MEMS micro-electro-mechanical systems

MicroMAS Micro-sized Microwave Atmospheric Satellite

MOPA Master Oscillator Power Amplfier

NIR   near-infrared

NODE Nanosatellite Optical Downlink Experiment

OCSD Optical Communication and Sensor Demonstration

OCTL Optical Communication Telescope Laboratory

OLI   Operational Land Imager

OPALS Optical Payload for Lasercom Science

PDF   probability density function

PI   proportional-integral

PSF   point-spread function

QE   quantum efficiency

RF   radio frequency

ROI   region of interest

SSTP Small Spacecraft Technology Program

STARlab Space Telecommunications, Astronomy, and Radiation laboratory

SWaP size, weight, and power

TIRS Thermal Infrared Sensor

TLE   Two-Line Elements

USGS U.S. Geological Survey

UV   ultraviolet

THIS PAGE INTENTIONALLY LEFT BLANK

Chapter 1

Introduction

1.1 Laser Communication

Laser communication is one of the key technologies capable of providing high-rate communication links, necessary to meet the growing communication demand of spacecraft. With more advanced space-borne scientific instruments, many spacecraft are capable of collecting significant amounts of data to be downlinked to the ground stations. However, due to limitations in number and duration of ground passes as well as limited on-board memory storage, traditional radio-frequency systems are falling short in meeting the increasing communication demand of spacecraft. Figure 1-1 shows the communication data trend of Earth-orbiting satellites, projecting that multi-gigabits per second link rate will be needed in the near future.

Free-space laser communication utilizes laser beam propagation in free space as the signal carrier, providing wireless communication links between the transmit and receive optical terminals [2]. The carrier wavelength for space applications is often in the visible to short-infrared range within the atmospheric window, as shown in Figure 1-2. Due to the difference in wavelength, laser communication is capable of providing higher data rate with a more compact and power-efficient system in comparison with traditional radio-frequency (RF) systems. The advantages of laser communication are enabled by the laser narrow beamwidth, high communication bandwidth with fewer spectrum regulations [1, 2, 3].
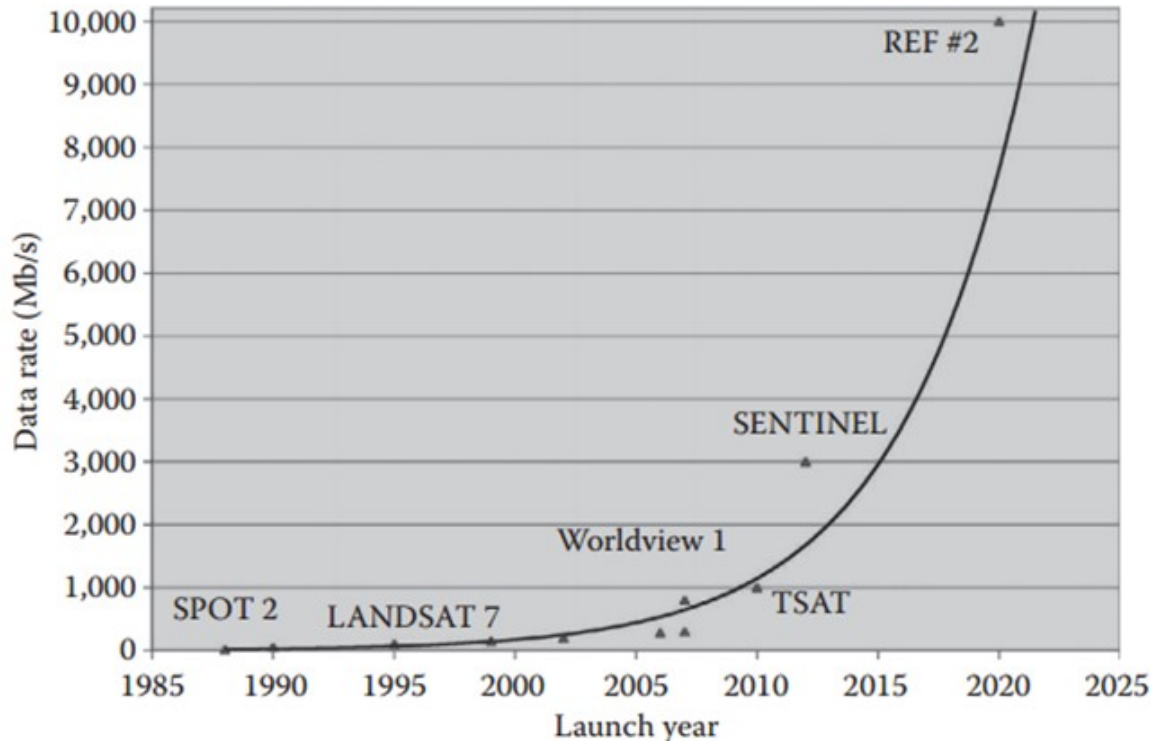
Figure 1-1: Data-rate trend for Earth-orbiting spacecrafts, showing a demand of multi-gigabits per second link rate in the near future [1]

In laser communication, data is modulated in low-divergence laser beams, made possible by the diffraction property of electromagnetic waves. The diffraction theoretical limit states that the beam divergence of electromagnetic wave is proportional to the wavelength and inversely proportional to the aperture diameter [5]. Since the wavelength used in laser communication is in the order of microns, much shorter than RF wavelengths, laser beams can achieve a divergence angle orders of magnitude narrower than RF beamwidths. Figure 1-3 illustrates the beamwidth difference of laser and RF communication systems, showing the RF footprint spanning continents while the laser spot size is approximately the size of a small city. As a result, laser communication systems provide more link directionality, lowering the required transmit power with the use of smaller transmit and receive apertures.

Other advantages of laser communication include high signal bandwidth, few spectrum regulation, and channel security. Because of the high carrier frequency of optical signals, the bandwith-to-frequency ratio for optical channels is orders of mag-
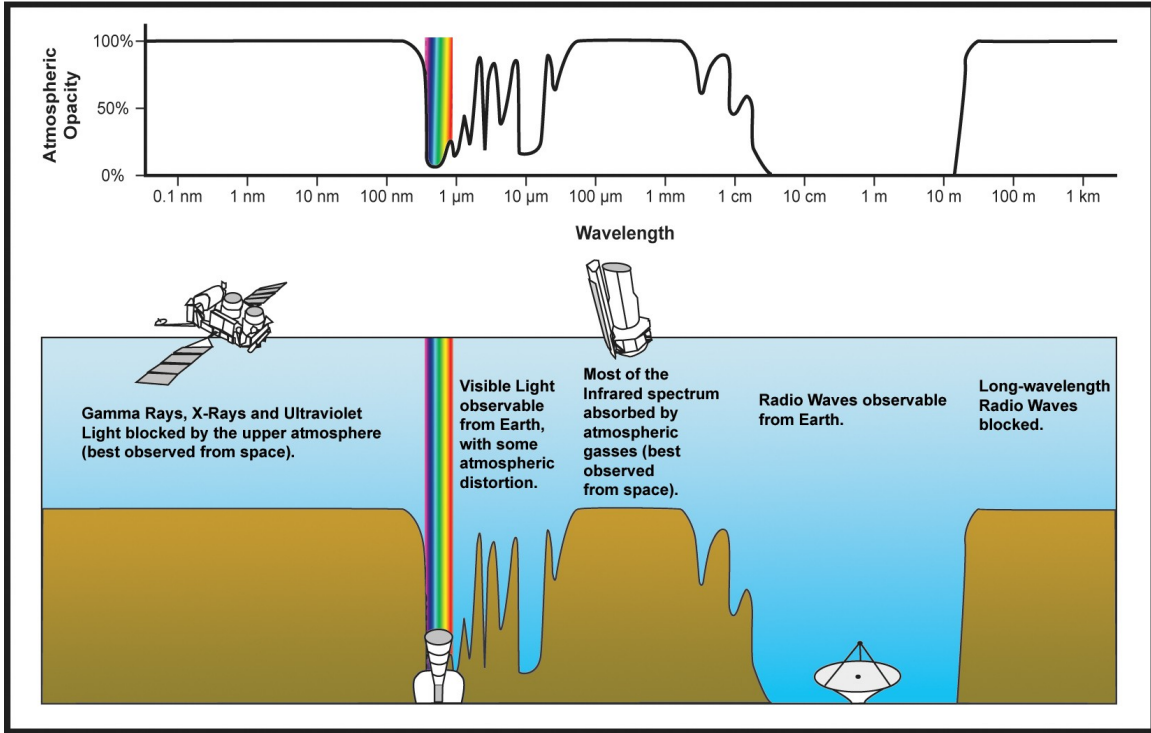
Figure 1-2: Earth's atmospheric transmittance of various wavelengths of the electro-magnetic spectrum, showing atmospheric windows in the visible/infrared and radio range [4]
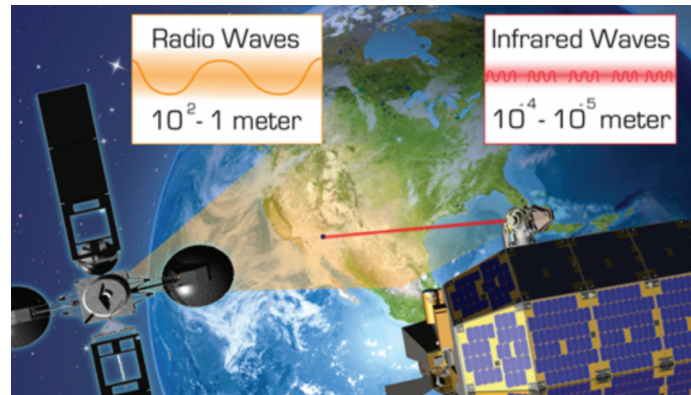
Figure 1-3: Laser communication footprint compared to traditional RF communica-tion footprint, showing the directionality of laser communication in comparison with RF systems [6]

nitude lower than for RF, providing much larger channel capacity [5]. In addition, while the RF spectrum is heavily regulated by national and international adminis-trations, optical links are not currently subjected to spectrum allocation, providing

more bandwidth availability and a simpler licensing process [1]. Furthermore, narrow laser beams offer increased link security, necessary for wireless transfer of sensitive information [2].

Limitations of laser communication are primarily from weather effects and pointing requirements. Absorption due to cloud and fog presents significant attenuation of laser signals, which could cause black-out periods where no laser link is available [1]. The locations of optical ground stations are, therefore, more selective than RF ground stations due to weather condition criteria. In addition, due to the low-divergence laser beamwidth, laser communication requires the spacecraft to maintain accurate pointing at the ground station for the link to be established. The pointing accuracy required corresponds to a fraction of a beamwidth such that most of the optical power can be received by the ground station. Since the high data-rate provided by laser communication is realized by the narrow beamwidth, better pointing accuracy is a direct indication of a higher data rate communication capability for laser communication systems.

1.2   CubeSats

Small satellites are among the fastest growing classes of satellite in the last decade because of low cost components, short development time, and availability of launch opportunities. Hundreds of satellites with mass of 1-50 kg have been launched in the past few years, with a steep increase in number expected in the upcoming years [7]. Figure 1-4a shows the number of small satellites launched from the year 2000 to 2013, showing a significant increase in the number of 1-10 kg satellites in recent years. Many of the launched small satellites are CubeSats, a popular class of miniaturized satellites, often used for technology demonstration and educational purposes. The number of CubeSats launched in the past decade is shown in Figure 1-4b, consistent with results in Figure 1-4a [8].

CubeSats have strict size and weight requirements, specified by the CubeSat program at the California Polytechnic State University, San Luis Obispo. One standard
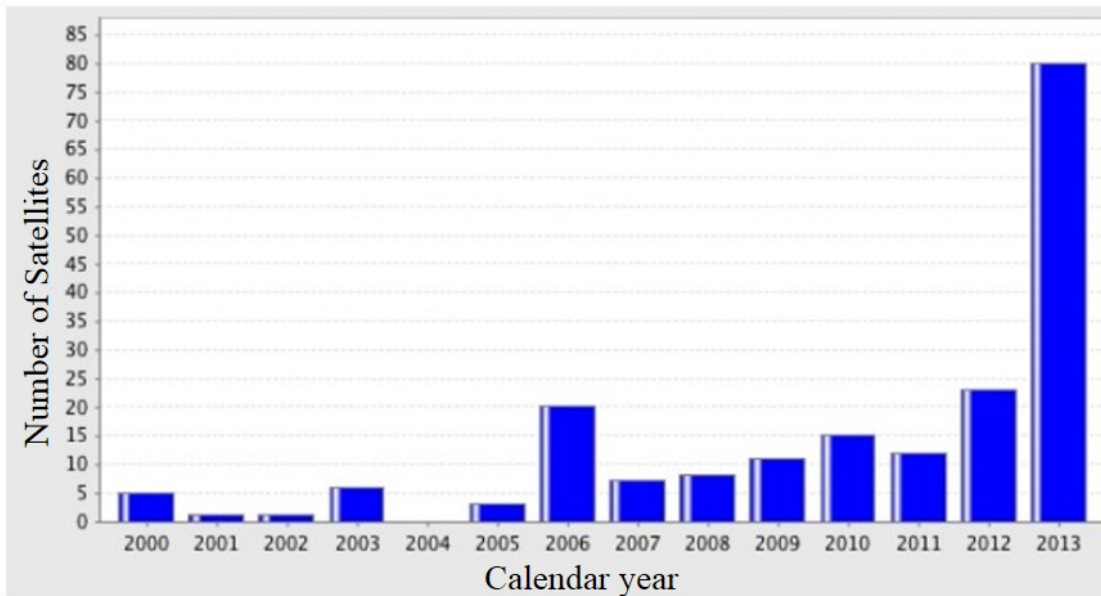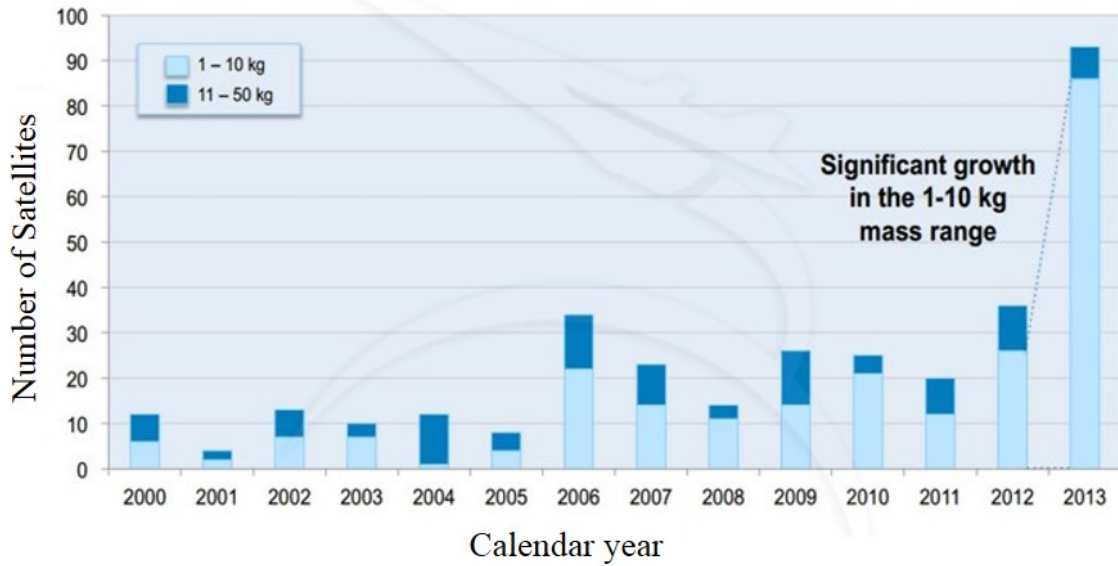
Figure 1-4: (a) Small satellites (1-50 kg) launched in 2000-2013 [7] (b) CubeSat-class missions launched in 2000-2013 [8]

CubeSat unit (1U) is 10 cm x 10 cm x 10 cm in volume and less than 1.33 kg in weight [9]. Common CubeSat sizes are 1U, 1.5U, 2U, 3U, as shown in Figure 1-5, with the size and weight requirements scaled correspondingly. The fully assembled Micro-sized Microwave Atmospheric Satellite (MicroMAS), a 3U CubeSat developed at MIT in the Space System Laboratory, is shown in Figure 1-6a. MicroMAS deployment from the International Space Station (ISS) in March 2015 is shown in Figure 1-6b, along

with a 1U CubeSat from the same deployer.

Image credit: CubeSat Kit/Pumpkin, Inc.
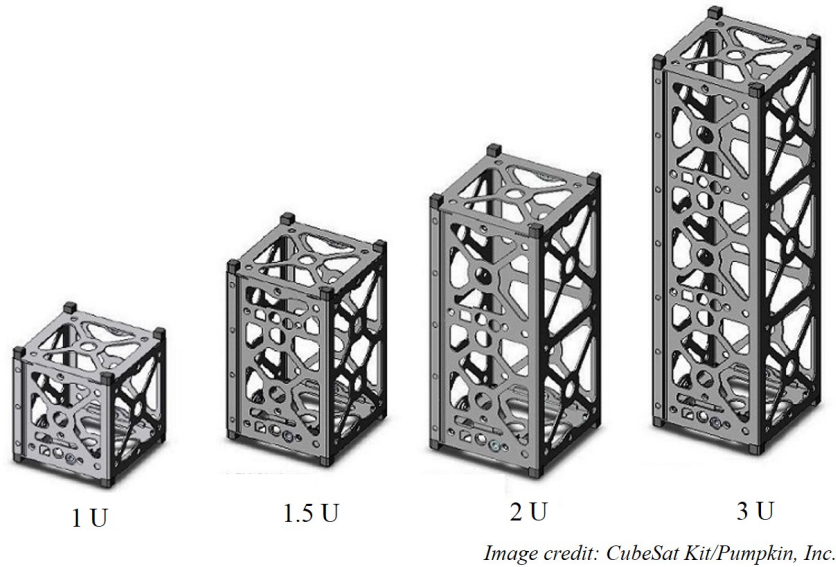
Figure 1-5: Common CubeSat-bus 3D models [10]
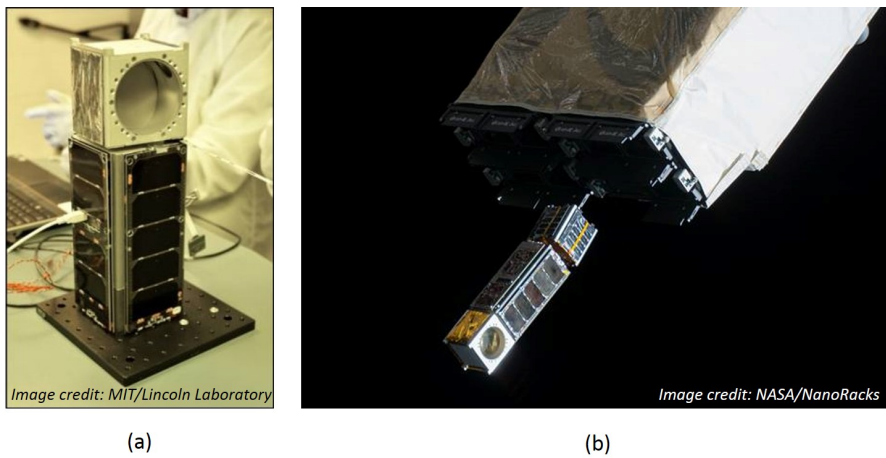
Figure 1-6: (a) The fully assembled MicroMAS during integration and testing (b) MicroMAS deployment from the ISS

New advances in CubeSat's system-level design, improvements in attitude control and onboard processing, as well as the desire to obtain persistent observations mean that a significant amount of data will be produced [11, 12, 13]. The amount of data successfully collected from a CubeSat mission is often limited by low-rate RF downlinks. Most CubeSats are in low-Earth orbit (LEO), which results in short ground station access times (<10 min/pass). The amount of downlinked data is

26

limited due to the low gain nature of RF communication systems and CubeSats' size and weight constraints. CubeSat RF communication capabilities in 2009-2012 are summarized in Figure 1-7, indicating that a majority of CubeSat RF systems achieve less than 1 Mbps data rate.[14] While RF downlink capability can be improved by having more ground stations or larger apertures with higher gain, these options are often expensive. In addition, RF systems have a heavily regulated licensing process due to the crowded frequency spectrum allocation, introducing the risk of schedule slip and cost. Thus, there is a growing demand in the nanosatellite community for higher rate downlinks with less regulatory complexity and lower cost, leading to the research and development of laser communication technology on CubeSat platforms in this work.
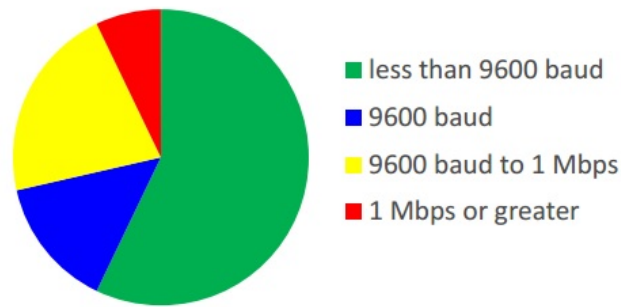
Figure 1-7: Survey results of CubeSat communication capabilities [14]

While advancements in satellite attitude determination have led to the development of several CubeSat-sized attitude sensors capable of achieving fine attitude knowledge, there is no existing sensor product that can achieve accurate pointing relative to a ground target, sufficient for laser communication. Devices such as star trackers are capable of achieving sub-milliradian attitude knowledge, realized by star field imaging techniques[15]. However, accurate attitude knowledge in inertial space does not guarantee accurate pointing knowledge relative to a ground target due to ephemeris uncertainty. For example, 1-km orbit ephemeris error of a satellite at 500-km altitude leads to an error of 0.1° in attitude when converting from inertial to Earth-fixed frame. Many CubeSats do not have access to the Global Positioning System (GPS) receivers and have to rely on published Two-line Element (TLE) data

for orbit determination, which could lead to orbit knowledge uncertainty of several kilometers [16]. This induced error limits CubeSats that require accurate ground target pointing from leveraging attitude sensing capability from inertial-based attitude sensors.

1.3 Laser Beacon Tracking

1.3.1 Laser Beacon Tracking Overview

A technique used by previous laser communication missions to achieve high pointing accuracy at the optical ground station is to utilize an uplink laser beacon from the ground as a reference. Ground laser beacon detection allows the spacecraft to directly acquire the location of a ground target and use this information for ground-referenced attitude determination, such that laser communication can be established. In addition, ground laser beacons can be designed to enhance detection probability, which is not possible when natural light sources are used as reference. For instance, the laser beacon has a narrow-band spectrum, allowing band-pass filtering techniques to be implemented at the receive terminal to reduce background light interference, improving attitude sensing performance.

To achieve pointing accuracy for downlink optical communication, a laser beacon is transmitted from the optical ground station, often from the same facility as the downlink receive terminal. The laser beacon source is expanded through a telescope, which sets the divergence angle needed to cover the full range of spacecraft's position uncertainty. The beacon beam is propagated through Earth's atmosphere, where it is affected by atmospheric absorption and scattering as well as atmospheric turbulence. The beacon is received on the spacecraft's terminal by imaging optics and detector. The beacon image is processed by flight software to determine the spacecraft's attitude relative to the beacon direction. For mono-static systems, where the beacon receiver and transmit laser are on the same actuated platform, the actuators are used to drive the platform until the beacon image is at a desired location, for example, at

the center of the detector as a feedback mechanism to ensure the downlink beam points accurately at the ground station. For bi-static systems, where no feedback is available, downlink pointing offset is computed from the beacon image through the geometric relationships of the beacon receiver and downlink platforms. Many optical communication systems are built with multiple attitude control stages to achieve the required pointing accuracy.

1.3.2   Literature Review

Laser beacon detection techniques have been utilized for several laser communication missions, such as the Laser Lunar Communication Demonstration (LLCD), the Optical Payload for Lasercom Science (OPALS), and the Optical Communication and Sensor Demonstration (OCSD). The LLCD and OPALS modules are on large space platforms, while the OCSD payload is carried by 1.5U CubeSats [17, 18, 19].

The LLCD mission, developed by NASA and MIT Lincoln Laboratory, established the first laser communication link from lunar orbit, achieving a record-breaking downlink data rate of 620 Mbps.[17] The Laser Lunar Communication System (LLCS), developed in the LLCD mission, was flown on the Lunar Atmospheric and Dust Environment Explorer (LADEE) spacecraft, launched in September 2013. The LLCS achieves a pointing accuracy of 2.5 μm during normal operations with the use of an uplink beacon for coarse tracking and piezoelectric actuation of the transmit fiber for fine stabilization. A 3D sketch of the LLCS optical module is shown in Figure 1-8a. The module weighs approximately 30 kg and operates at an average power of 50-140 W. The 10-cm aperture Cassegrain telescope and back-end optics are mounted on a two-axis inertially stabilized platform. The optical layout is shown in Figure 1-8b, illustrating the three-wavelength design, with separate uplink acquisition beacon and communication wavelengths and a downlink communication wavelength. The three distinct wavelengths are within the range of 1550 nm-1570 nm. The uplink beacon, shown in green, is separated from the uplink and downlink communication beams by a dichroic mirror after being received through the main telescope mirrors and tertiary lens. The beacon is then focused onto an acquisition InGaAs quadrant detector

through an acquisition lens system. The acquisition lens and sensor provides a field of view of greater than ±1 mrad, sufficient to accommodate spacecraft's pointing uncertainty and jitter before beacon acquisition. [17, 20]
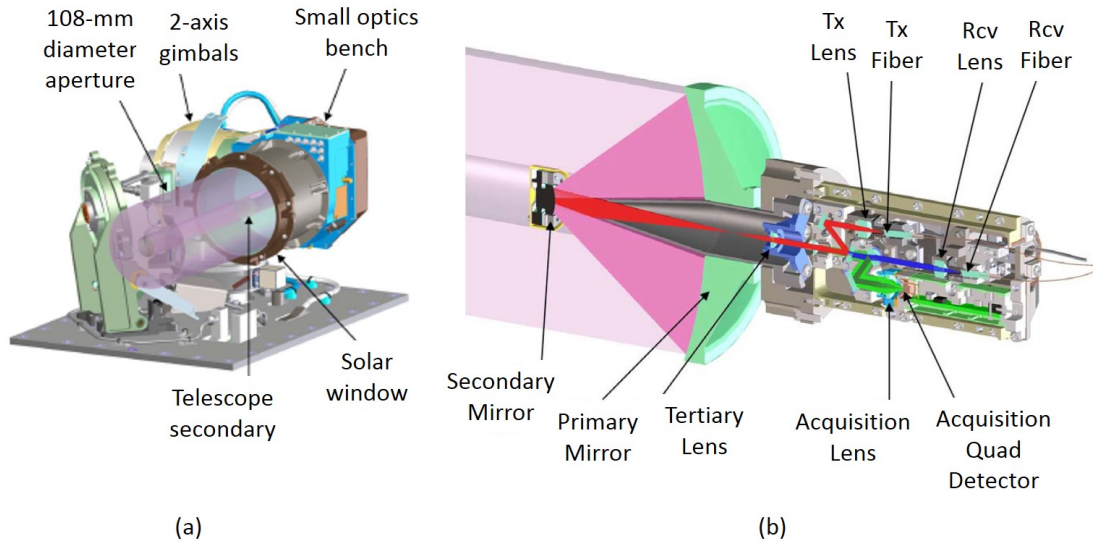
Figure 1-8: (a) 3D model of the inertially stabilized telescope for the LLCD (b) LLCD optical layout with three distinctive beam paths for the uplink beacon, uplink communication, and downlink communication [20]

In April 2014, the OPALS system was launched on a SpaceX Dragon commercial resupply capsule to carry out a 90-day baseline optical downlink mission. The OPALS mission is developed by the Jet Propulsion Laboratory to establish an optical communication link from the ISS to the Optical Communication Telescope Laboratory (OCTL) facility at Table Mountain, CA. The mission aims to provide a downlink rate of 30-50 Mbps at 1550 nm with the use of an uplink beacon at 976 nm for acquisition and tracking. An illustration of the OPAL communication operation from the ISS is shown in Figure 1-9a. The flight system is shown in Figure 1-9b, consisting of three main components: the sealed electronics container connected to a radiator, the optical head mounted on a two-axis gimbal, and the top half of the Flight Releasable Attachment Mechanism (FRAM) [18].

The laser communication system achieves a pointing accuracy on the order of 300 μrad (1-σ), sufficient to decode the transmit optical signal. This pointing accuracy is accomplished by the use of a laser beacon transmitted from OCTL at 976 nm. The

30
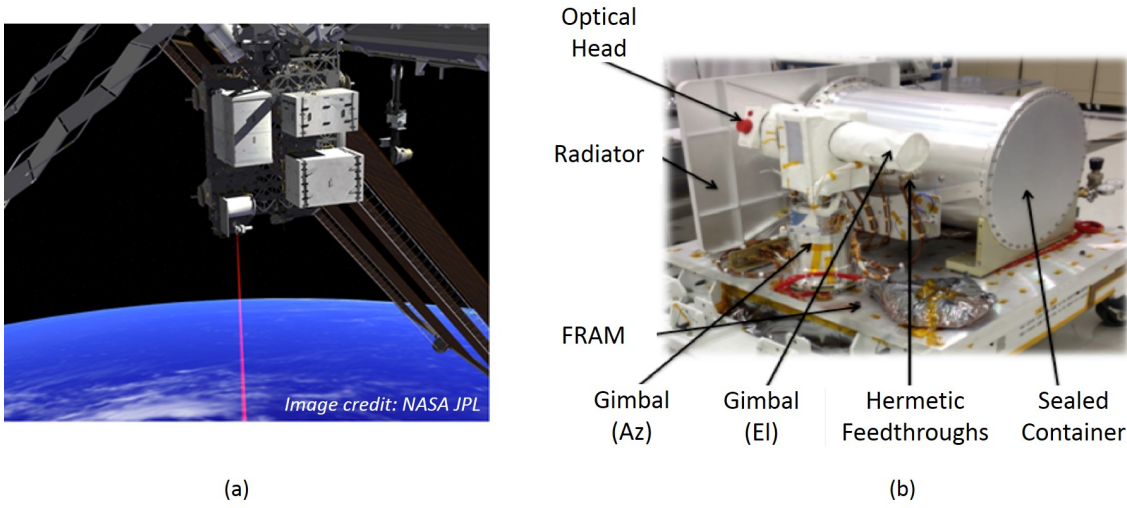
Figure 1-9: (a) Artist concept of the OPALS payload during on-orbit operation (b) OPALS flight system layout [18]

beacon is acquired by a commercial off-the-shelf charge-coupled device (CCD) camera, mounted on a two-axis gimbal. The CCD camera has a resolution of 640 x 480 pixels, running at a frame rate of 100 Hz. The beacon is detected when the intensity exceeds a threshold and centered on the center of the CCD using a Proportional-Integral (PI) control algorithm for ground station tracking. [18, 21]

The OCSD mission will be the first optical communication mission demonstrated on miniaturized satellite platforms. OCSD is a two-CubeSat flight test developed by the Aerospace Corporation, selected by NASA's Small Spacecraft Technology Program (SSTP) to be launched in late 2015. The OCSD baseline mission is to establish an optical communication link of 5-50 Mbps from the satellite in LEO to a 30-cm diameter telescope at Mt. Wilson in Southern California. The design of each OCSD 1.5 U CubeSat is shown in Figure 1-10. The OCSD CubeSats utilize a combination of coarse and fine sensors to accomplish a pointing accuracy of 0.1°, sufficient to meet the pointing requirement imposed by the downlink beamwidth. The coarse sensors include six 2-axis sun sensors, four Earth horizon sensors, a two-axis nadir sensor, and two sets of 3-axis magnetometers. The coarse sensor suite is capable of achieving continuous attitude knowledge to 1° accuracy. Fine attitude determination is accomplished by close-loop tracking of a 10-W uplink beacon at 1550 nm. The up-

31

link beacon detector is a 3-mm diameter InGaAs quad photodiode, accompanied by a 18-mm lens system and narrow-band filter. The fine attitude determination system with laser beacon detection can achieve an accuracy of 0.1° in attitude knowledge. [22, 19]
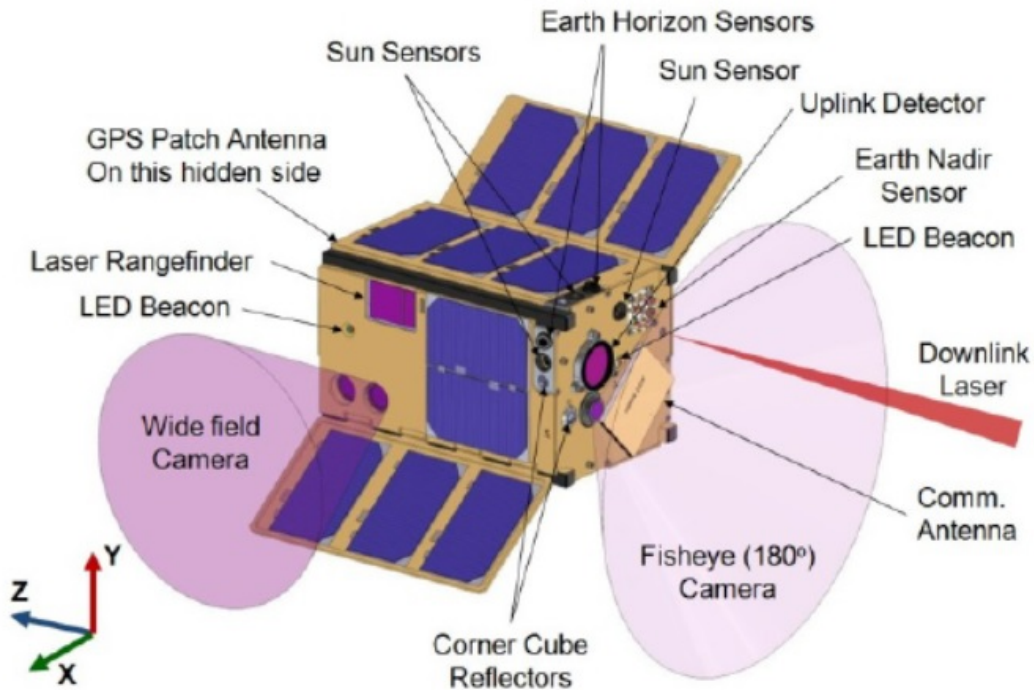
Figure 1-10: 3D rendering of the OCSD CubeSat system [19]

1.3.3 Thesis Overview

The work presented in this thesis includes the design and development of a CubeSat-sized laser beacon receiver to support the Nanosatellite Optical Downlink Experiment (NODE), currently under development in the MIT Space Telecommunications, Astronomy, and Radiation (STAR) laboratory. NODE aims to establish a laser communication downlink at 10-50 Mbps from a CubeSat in LEO. NODE uses a two-stage pointing control mechanism to achieve pointing performance of $\pm$ 0.09 mrad 3-σ without bias, sufficient for a 2.1 mrad downlink laser.

With better pointing accuracy and narrower downlink beam, NODE aims to achieve a data rate comparable to OCSD with less power consumption because of higher link efficiency. The coarse stage relies on the host spacecraft body pointing capability while the fine stage is driven by a miniature MEMS fast-steering mirror. Precise attitude sensing is accomplished by the use of a beacon receiver system in addition to common CubeSat attitude sensors such as sun sensors, magnetometers, and Earth horizon sensors. The hand-off between coarse and fine control is achieved by sizing the beacon camera's field-of-view to compensate for the satellite's body control capabilities under on-orbit disturbances. The NODE module will fit within a 0.5 U volume, weigh less than 1 kg, and consume no more than a total of 10 W of electrical power during active communication periods, meeting CubeSat size, weight, and power (SWaP) constraints.[23]

Since the mission success relies on the ability to achieve accurate ground station pointing, the NODE beacon receiver system is an integral part of the system as it is responsible for providing the fine attitude knowledge needed to meet the pointing requirement for laser downlink while maintaining low size and mass to meet CubeSat constraints. The NODE beacon receiver is capable of achieving an attitude knowledge of better than 0.1 mrad with low probability of fade under a variety of sky brightness conditions and orbit configurations. The beacon receiver system consists of low-cost commercial off-the-shelf (COTS) detectors, lens, and filters, leading to a total equivalent size and mass of 0.1 U.

The following chapters of this thesis will present the design of the beacon camera of the NODE configuration along with simulation development and results to validate the system performance. Chapter 2 will introduce the high-level overview of the NODE system along with the current camera design and hardware selection. Chapter 3 will detail an end-to-end beacon simulation to construct expected beacon image frames with transmitter, receiver, and atmospheric channel properties taken into account. The simulation results and corresponding attitude determination performance of the module will be presented in Chapter 4. Chapter 5 will summarize the findings, discuss future development efforts, and present the significance of this research.

THIS PAGE INTENTIONALLY LEFT BLANK

Chapter 2

Approach

2.1 System Overview

2.1.1 System Architecture

The NODE system is a CubeSat-size communication module, designed to establish a 10-50 Mbps laser communication downlink from LEO. NODE uses a 2-W laser at 1550 nm with 2.1 mrad (0.12°) beam divergence to support the communication link. An uplink beacon at 850 nm is transmitted from the ground station to provide precise ground station acquisition and tracking. In addition to the primary laser downlink, the NODE architecture also includes a low-rate bi-directional RF link for telemetry, command, and back-up transmission when the laser link is not available. The NODE architecture is summarized in Figure 2-1.

The mission concept of operations for a ground pass consists of three main phases, as illustrated in Figure 2-2 and detailed in Table 2.1. First, the satellite slews autonomously at the ground station using coarse attitude sensors and actuators. The pointing accuracy of the coarse system is expected to be within ±3°, sufficient for the beacon to be within the onboard beacon camera's field-of-view. Next, as the beacon is acquired, the satellite continues to slew toward the ground station using coarse-stage actuators to align the body-mounted beacon camera boresight with the ground beacon, reducing the pointing error to approximately better than ±1°. Lastly, the

fine-pointing mechanism is activated, steering the downlink laser beam toward the ground station within a pointing accuracy of $\pm 0.06°$, which corresponds to $\frac{1}{2}$ of the downlink beamwidth.
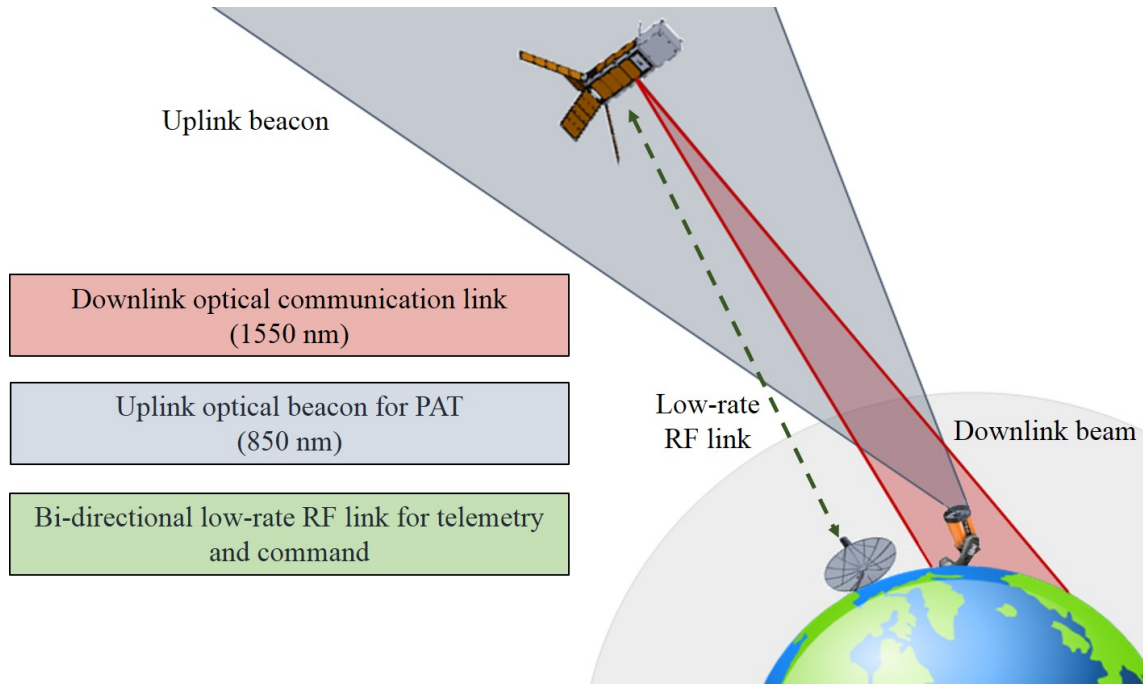
Figure 2-1: NODE system architecture, consisting of a 1550-nm downlink beam as primary downlink method, a 850-nm uplink beacon for acquisition and tracking, and a bi-directional radio-frequency link for telemetry and command [23]

2.1.2 NODE System Overview

The NODE spacecraft payload consists of two main subsystems: a downlink transmitter and an uplink beacon receiver. Due to size constraints, the payload uses a bistatic design, with separate downlink and uplink beacon paths. The physical layout of the payload is given in Figure 2-3. The transmitter design follows a Master Oscillator Power Amplfier (MOPA) architecture, where an Erbium Doped Fiber Amplfier (EDFA) is used in conjunction with a 1550 nm seed laser to provide a high peak-to-average power optical waveform. A fiber collimator forms the transmit beam which is subsequently directed by the fast-steering mirror (FSM) in a "gimballed-flat" topology. The selected FSM is a MEMS tip/tilt mirror that meets the SWaP require-
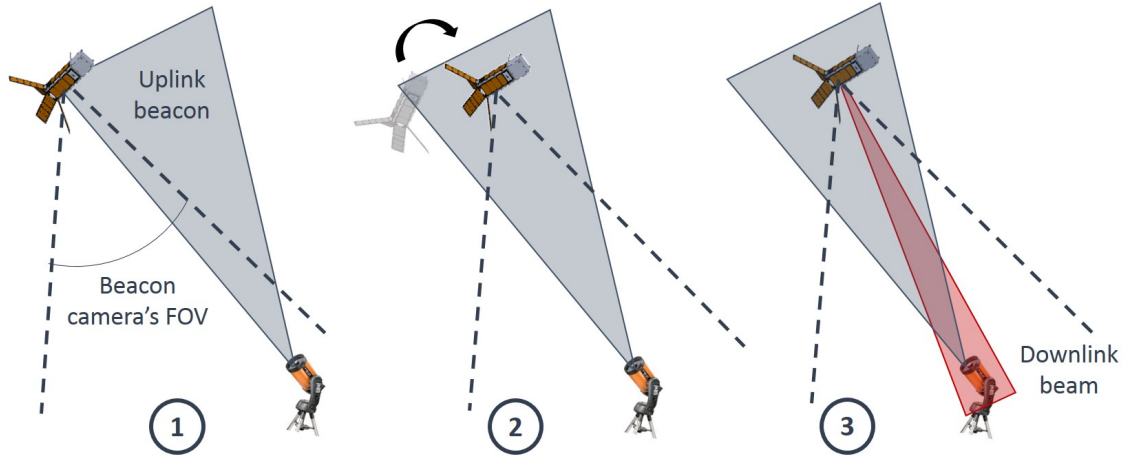
Figure 2-2: NODE concept of operations during each ground pass: (1) the satellite point autonomously at the ground station using coarse sensors and actuators, (2) the beacon is acquired, allowing the satellite to correct its attitude with coarse attitude control actuators, (3) Fine-pointing mechanism is activated, initiating the downlink process.

ments as well as the steering range needed for coarse stage hand-off. The beacon receiver camera consists of a complementary metal-oxide semiconductor (CMOS) focal plane array with high sensitivity in the near-infrared (NIR) range to detect a 850 nm beacon transmitted from the ground station. The uplink beam image is processed with centroiding algorithms for fine attitude determination.

Transmitter Overview

The NODE transmitter follows a MOPA architecture, consisting of a modulated seed laser source followed by a power amplifier. The MOPA configuration allows for high-rate modulation with high-fidelity waveform as and modularization such that each components can be designed and optimized independently [2]. The seed laser selected for NODE is a 6 dBm average power laser at 1550 nm with integrated thermoelectric cooler for wavelength stability. The components are part of a transmitter optical sub-assemblies (TOSA), available in compact fiber-coupled packages (20 mm x 8mm x 5mm), appropriate for low SWaP applications such as NODE. The seed laser is modulated directly through the use of a field-programmable gate array (FPGA) to generate the communication waveform following the pulse-position modulation (PPM) modu-

37

Table 2.1: NODE concept of operations and pointing accuracy requirements

1	**CubeSat slews toward ground station**	
	Sensors	CubeSat coarse sensors
	Actuators	CubeSat reaction wheels
	Pointing accuracy	$< 3°$
2	**CubeSat closes loop around beacon offset**	
	Sensors	Beacon camera
	Actuators	CubeSat reaction wheels
	Pointing accuracy	$< 1°$
3	**Fine steering mechanism is activated**	
	Sensors	Beacon camera
	Actuators	Fast-steering mirror
	Pointing accuracy	$< 0.06°$
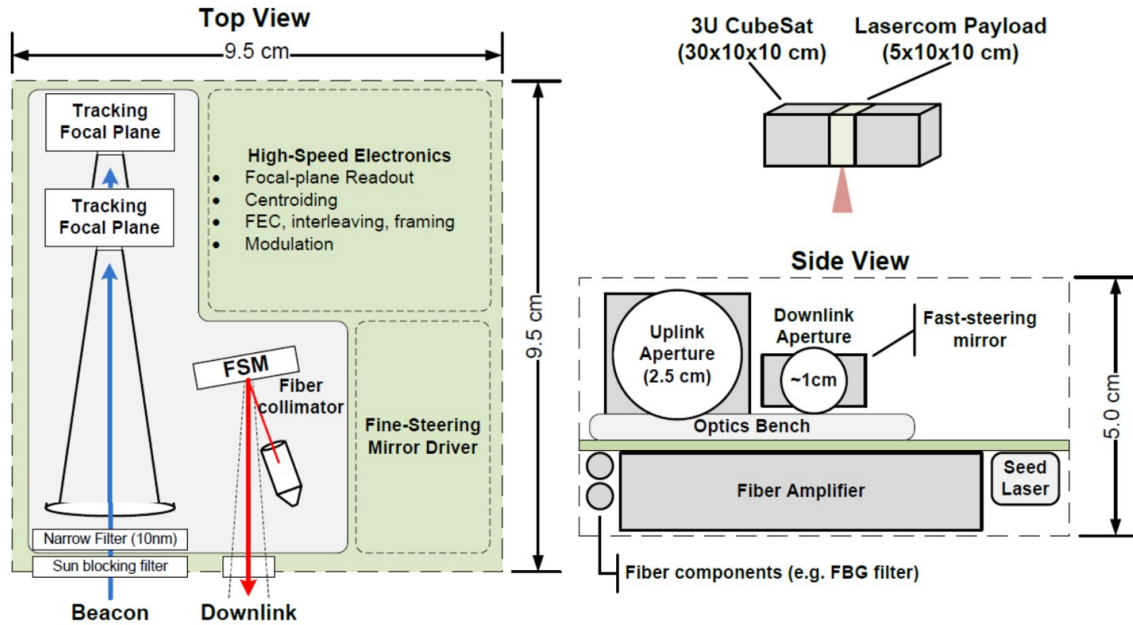
Figure 2-3: NODE physical system layout, showing the bi-static design with independent downlink and uplink beacon path [23]

lation scheme. To improve the extinction ratio (ER), an athermal fiber Bragg grating (FBG) bandpass filter centered at the seed laser transmission wavelength was used. The achieved ER is >33 dB, as measured in lab-bench hardware characterization. NODE utilizes an EDFA, advantageous for low-duty cycle and average-power-limited

applications. The EDFA module is approximately 9 cm x 6 cm x 1.5 cm and has an average power level of 200 mW. The NODE transmitter block diagram is shown in Figure 2-4.
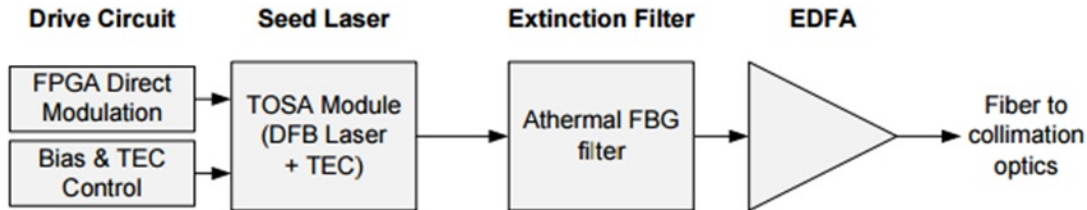
Figure 2-4: NODE transmitter block diagram following a MOPA design [24]

Coarse Stage Control

The coarse stage control is achieved through the host CubeSat's attitude determination and control system (ADCS). While NODE was designed to be mostly agnostic to the choice of host satellite choice of sensors and actuators, there are few requirements, as shown in Table 2.2, that the host CubeSat needs to meet such that the NODE module can be operated. First, the CubeSat's ADCS suite is required to achieve a pointing accuracy of better than $\pm 3°$, such that the ground laser beacon can be detected by the laser beacon camera on the satellite. This level of pointing accuracy is within the expected performance of existing CubeSat's actuators and sensors and has been achieved by a number of 3-axis stabilized CubeSats [25, 26]. Once the beacon has been acquired, which provides an attitude knowledge of better than 0.1 mrad, the CubeSat's control system is required to provide an control of better than $\pm 1°$in order to meet NODE's fine-stage control mechanism's range of operation. During the ground-pass, the CubeSat is required to provide a slew rate of up to $1°$/s to properly track the ground station, while performing attitude control with the accuracy requirements specified in the first two requirements.

Table 2.2: Host CubeSat ADCS requirements

Parameter	Requirement
Host ADCS-only pointing accuracy	± 3°
Pointing accuracy with beacon camera	±1°
Slew rate	up to 1.1°/s (orbit dependent)

Fine Stage Control

The fine-stage control is achieved by a micro-electro-mechanical systems (MEMS) fast-sterring mirror (FSM) from Mirrorcle Technologies, as shown in Figure 2-5. The tip/tilt range of the FSM is ±1.25°, overlapping with the CubeSat body pointing capability. The fine-stage pointing requirements are based on the beamwidth specifications, determined through detailed link budget analysis to achieve the goal data rate [27]. With a beamwidth of 2.1 mrad (0.12°), the 3-σ pointing accuracy requirement is set at ±1.05 mrad (±0.06°).
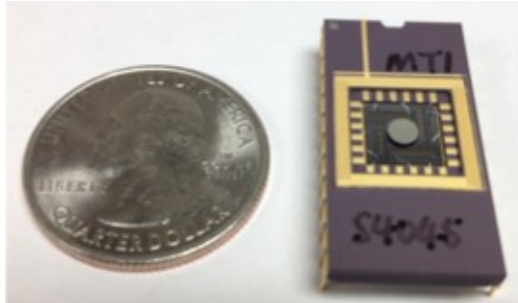
Figure 2-5: Fast steering mirror utilized in NODE from Mirrorcle Technologies, Inc.[23]

A simple setup was developed to characterize the device, as pictured in Figure 2-6 [28]. A 650-nm red laser is directed through a focusing lens, which the FSM steers into a CMOS monochromatic camera. From the geometry of the setup, the angle of the FSM can be determined. Since there is no feedback available on the device's position, it was necessary to characterize repeatability of the device to ensure it could meet performance requirements.

To test repeatability, the mirror was commanded to visit each of the points in a "5-sided die" pattern covering its entire range. For each iteration, as shown in the focal
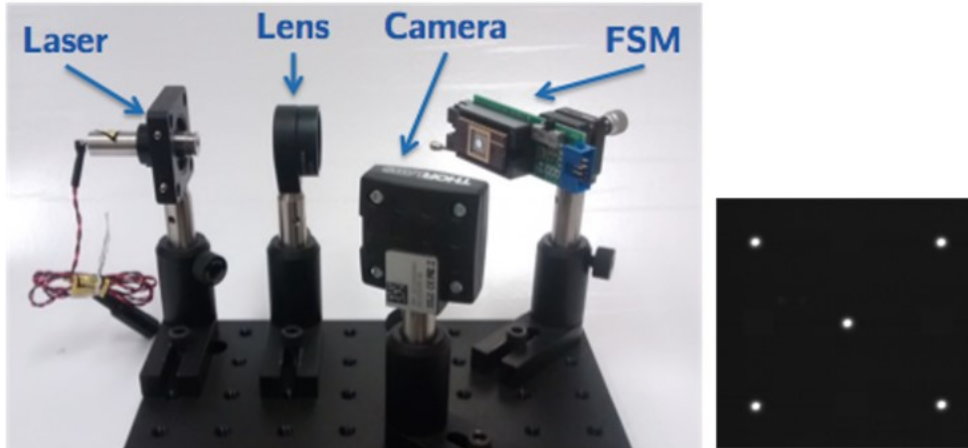
Figure 2-6: Experimental setup for FSM characterization (left)[28] and 5-sided die pattern used for repeatability analysis (right)[23]

plane in Figure 2-6, points were visited in a random order. Statistics on the position repeatability for a significant number of trials (N=500) show that the RMS error of the device is 12 μrad, well within the desired performance. Future testing will aim to ensure repeatability under varying thermal environments. Prior simulation analysis showed that the staged setup remains well within the accuracy requirement [27].

2.2 Laser Beacon System

2.2.1 Beacon Detection Architecture

The laser beacon tracking architecture consists of a laser source, transmitted from a ground station and detected by an on-orbit camera at the satellite terminal after propagating through the atmospheric channel. An illustration of the laser beacon tracking configuration is shown in Figure 2-7. The ground-based laser source is launched through a telescope, which determines the beam divergence angle necessary to cover the satellite's position uncertainty. The telescope is mounted on a steering platform, allowing continuous tracking of the satellite over each ground pass. The beacon wavelength was chosen to be in the NIR range to comply with eye-safety regulations while maintaining sufficient sensitivity with standard Silicon focal plane arrays, reducing

cost while increasing product availability. Laser propagation through the atmosphere is a complex process, leading to both attenuation from atmospheric absorption and scattering as well as brightness fluctuations due to the turbulent nature of the atmosphere. Upwelling Earth brightness presents the main source of background radiance, varying significantly based weather conditions and time of day. At the satellite terminal, the laser beam is detected by a beacon camera, consisting of a focal plane array, lens system, and filters. The camera's field-of-view (FOV) is chosen to be sufficiently wide to compensate for coarse attitude control capability while narrow enough to reduce the amount background light in the system. Filters are used to select the spectral band of the transmit laser and to reduce the effect of ultraviolet light in the optical system. Since the beacon is effectively a point source, the beacon image follows the point-spread function (PSF) of the lens system, sampled according to the resolution of the focal plane array. Once the beacon is detected by the camera, image processing techniques such as thresholding and centroiding can be applied to find the pixel location of the beacon image on the focal plane array. This information directly correlates to the direction of the beacon relative to the spacecraft's body coordinate system, providing ground-referenced attitude knowledge for the satellite.

2.2.2 Ground Segment Concept

The main design parameters of the ground system are the laser transmit power and beam divergence. In the system's baseline design, the transmit power is set at 10 W, where off-the-shelf laser diodes and drivers are available, reducing fabrication cost. This power level is comparable with existing beacon laser transmitter system at the Optical Communication Telescope Laboratory (OCTL) at JPL's Table Mountain Facility[29]. The beacon beamwidth is sized to accommodate the satellite's ephemeris error, which can be approximately 10 m - 2 km, accomplished with ranging systems such as GPS receivers and ultra-high frequency (UHF) radio ranging [19, 13]. For the baseline design, the ground laser beamwidth is set to be 5 mrad FWHM, necessary to cover a 2-km range as projected onto a 400-km orbit at zenith. The baseline transmit power and beam divergence design complies with the maximum permissible exposure
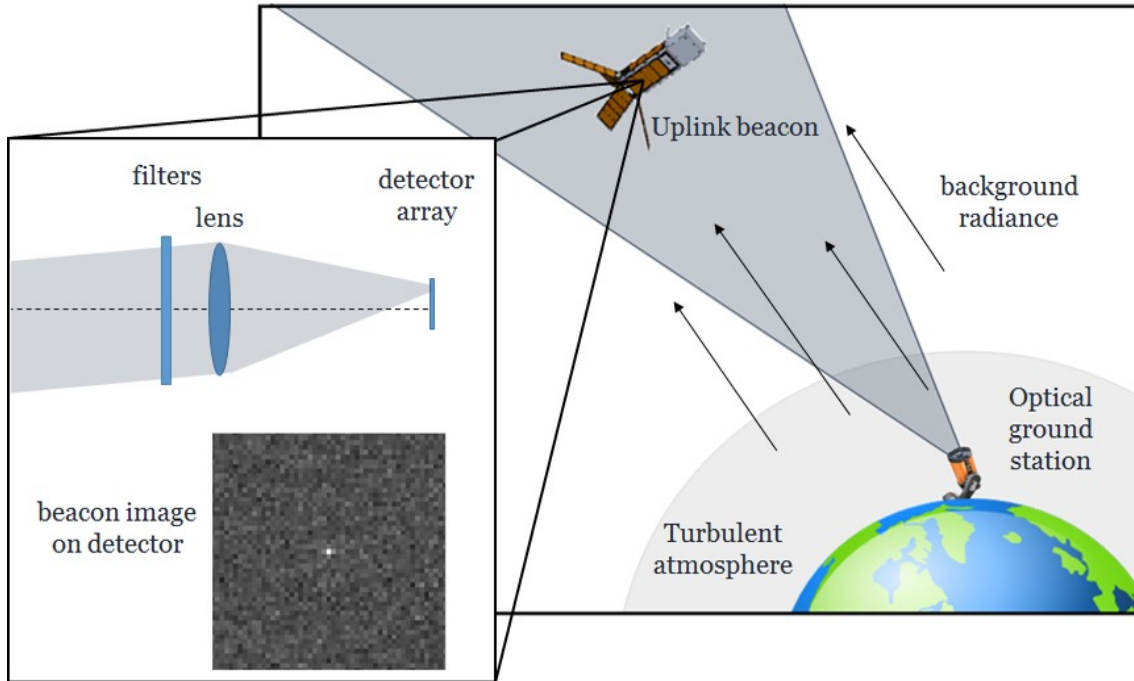
Figure 2-7: Overview of NODE laser beacon detection architecture. The laser beacon is transmitted through a telescope, propagating through the atmosphere, before getting detected by the beacon camera. The beacon image on the detector is affected by background radiance as well as atmospheric turbulence.

(MPE) limit advised by the Federal Aviation Administration (FAA) to ensure aviation safety [30].

2.2.3 Beacon Camera Prototype Development

Hardware Design Overview

The beacon camera design goal is to achieve sufficient beacon signal-to-noise ratio for detection while maintaining a small form factor to meet CubeSat's size and mass constraints. A secondary goal is to keep the module at a low cost, which led to the decision of using only COTS products. The system is designed to detect a laser beacon at 850 nm, a common NIR wavelength at which many laser and optical components are available. The current beacon camera prototype is shown in Figure 2-8. The system size is approximately 40 mm x 40 mm x 60 mm with a total weight of 120 g.

The beacon camera prototype consists of a focal plane array, lens system, band-

Figure 2-8: CubeSat-sized laser beacon camera utilized in NODE for ground tracking

5 Mpixel camera with
integrated band-pass filter

f/1.4 lens system   UV/VIS-cut filter

Figure 2-9: Laser beacon camera components, consisting of a 5 MP detector, 35 mm lens system, band-pass and long-pass filters

pass filter, and long-pass filter. To reduce cost and expand the option pool, a standard CMOS Silicon detector array was selected. The lens system is a 1-inch aperture off-the-shelf product with a focal length that provides a FOV wide enough to compensate for expected pointing error from CubeSat coarse attitude control. Two optical filters are utilized in the system: a band-pass filter at the beacon wavelength and a long-pass filter to protect the lens system from heating and darkening due to solar radiation. Table 2.3 summarizes the detailed specifications of the beacon camera. Detailed descriptions of the individual components are described below.

Table 2.3: Beacon camera specifications

Detector array	
Sensor format	1/2.5 in
Resolution	5 MP
Pixel size	2.2 μm
Quantum efficiency (at 850 nm)	15%
Lens	
Aperture diameter	1 in
Focal length	35 mm
Filters	
Band-pass filter transmission	(850 +/- 5) nm
Long-pass filter transmission	>700 nm

Detector

The main parameters considered during the detector selection process include array format, sensitivity, and noise properties, as well as cost, availability, and size. CMOS detectors offer cost-efficient solutions thanks to recent development in digital imaging and semiconductor chip production. With lower fabrication cost, CMOS detectors are often less expensive than their counterparts, CCDs. The CMOS commercial market has expanded significantly, providing a wide selection of sensor array format. Despite having peak sensitivity in the visible range, many low-cost and commercially available CMOS detectors have non-negligible quantum efficiency in the NIR range, approximately 10% - 30% at 850 nm depending on the target applications [31, 32, 33]. While CMOS sensors often produce higher noise in their image than CCD sensors, this noise level is negligible compared to background noise sources, as will be shown in later chapters.

Through many design iterations, a 5-Megapixel detector from Aptina Imaging was selected because of its high resolution, high sensitivity at 850 nm, as well as low dark current and read noise properties. The Aptina detector layout is presented in Figure 2-10a, showing an active area of approximately 2592 x 1944 pixels. With 2.2 μm pixel size, the equivalent active area is about 5.7 mm x 4.3 mm. The camera's quantum efficiency at 850 nm is approximately 15%, sufficient for beacon detection.

Dark current noise and read noise for this sensor is less than 100 LSB/s and 10 LSB, respectively, with the transaction factor of approximately 0.5 LSB/e- at low gain.

The Aptina chip was packaged into a compact and inexpensive commercial camera module by Matrix Vision in the MvBlueFOX-MLC series, shown in Figure 2-10b. The camera module is 35 mm x 33 mm x 25 mm without lens and weight approximately 10 g. The module has a USB 2.0 interface and can be integrated for use with ARM-based embedded boards.
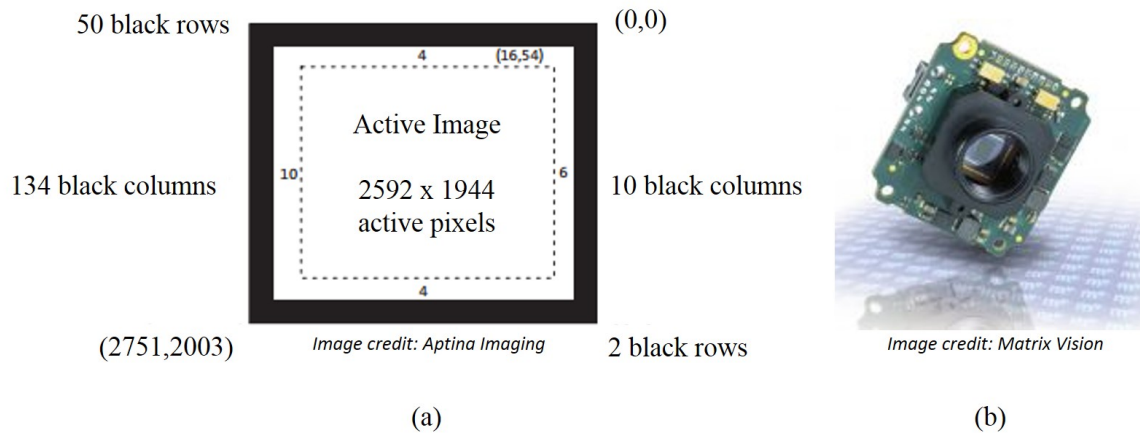
Figure 2-10: (a) 5 MP Aptina sensor format (b) Miniaturized camera module from Matrix Vision

Lens

The lens system was selected to provide the required field of view of the system with low aberrations while maintaining a small size to comply with CubeSat constraints. To meet the coarse pointing capability of $\pm 3°$, the camera's FOV is required to be greater than 6° full angle. Since the shorter dimension of the detector is 4.3 mm, the focal length requirement of the system can be found to be less than 41 mm, following the relationship shown in Figure 2-11. To ensure a beacon detectability across the field of view, the lens system needs to maintain a high brightest pixel flux fraction at various field angles, often achieved by multiple-element lens system so that aberrations can be corrected. Larger lens aperture provides larger photon collection area and higher gain for the beacon detection system. However, due to the 0.5U size

constraint for the entire NODE module and packaging of other components, the lens aperture is restricted to be approximately 1" or less.
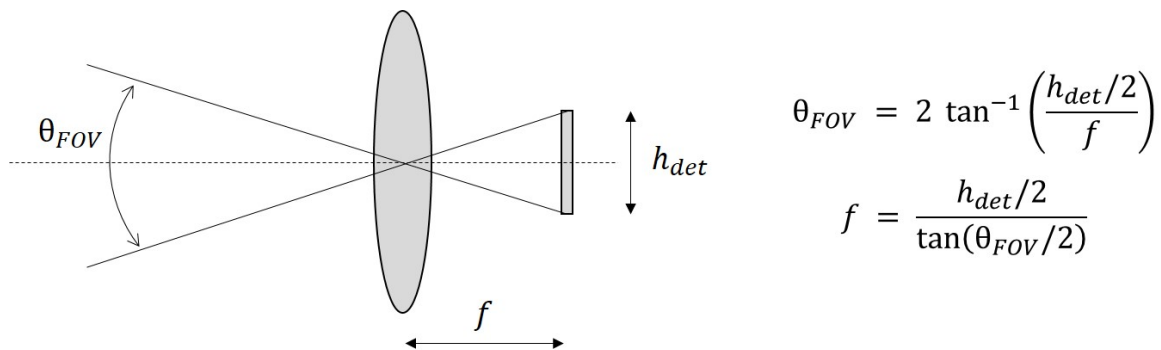
Figure 2-11: Illustration of system field-of-view and lens focal length

$$\theta_{FOV} = 2 \, \tan^{-1}\left(\frac{h_{det}/2}{f}\right)$$

$$f = \frac{h_{det}/2}{\tan(\theta_{FOV}/2)}$$

The lens system selected for the beacon camera lab-bench prototype is the *35mm VIS-NIR Compact Fixed Focal Length Lens* from Edmund Optics [34]. The lens system is of 1-inch diameter optics format with approximately 21 mm of clear aperture. The lens system consists of 7 optical elements made of a combination of glass materials with coating specified for the wavelength range of 425 - 1000 nm. The lens system has an outer diameter of 33 mm, physical length of 41 mm, and a total weight of 75 g. It is noted that the Edmund Optics lens system is not vacuum-compatible and will not be used for flight without modifications. Other lens systems considered for flight are shown in Appendix A.

The optical properties were analyzed through a "black-box" ZEMAX lens model provided by the vendor. Figure 2-12a shows the lens system layout, consisting of 2 main components, with detailed components and design hidden for proprietary purposes. The effective field of view of the system is 6.6° × 8.7°, as defined by the lens properties and detector's active area. Figure 2-12b shows the equivalent Seidel coefficients of the two components, showing spherical and coma as the most significant aberrations. Figure 2-13 shows the PSF on axis and at (0.0°,3.3°), (3.3°,0.0°), and at (3.3°, 3.3°), generated using the Fast-Fourier Transform (FFT) PSF feature of ZEMAX analysis tools. In all the field angles within the system's field of view, there is at least 9% of energy enclosed within a square of 2.2 μm (1 pixel) in the focal plane of the system. This means that at least approximately $\frac{1}{10}$ of the received optical

power is focused in one pixel.
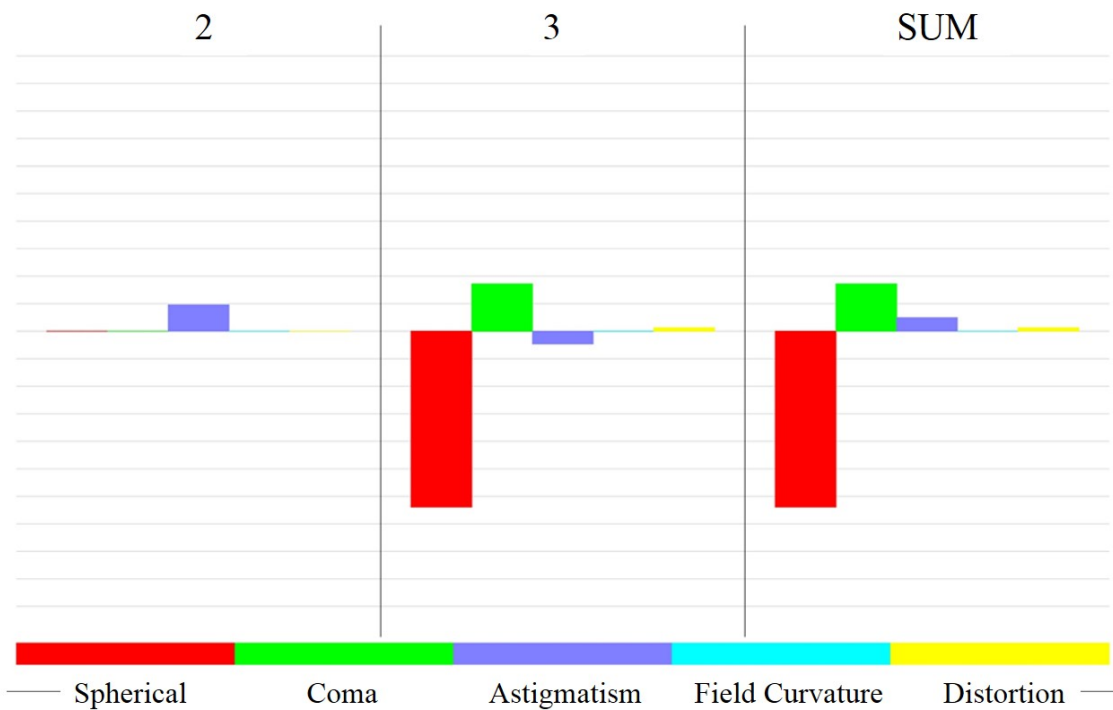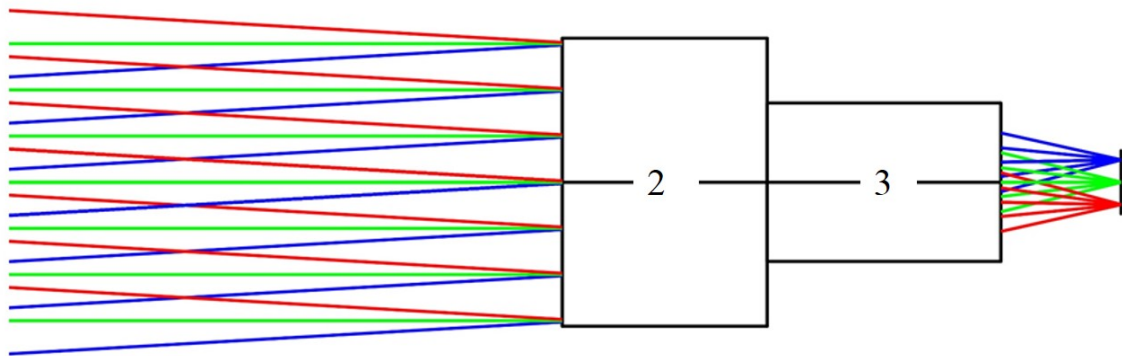
Figure 2-12: Edmund Optics lens system ZEMAX model and corresponding Seidel diagram

Filters

Band-pass filter   The beacon system requires narrow band-pass filtering to limit the amount of background noise in the system and improve the signal-to-noise ratio for beacon detection. The background sky spectral radiance at 850 nm will be further

48
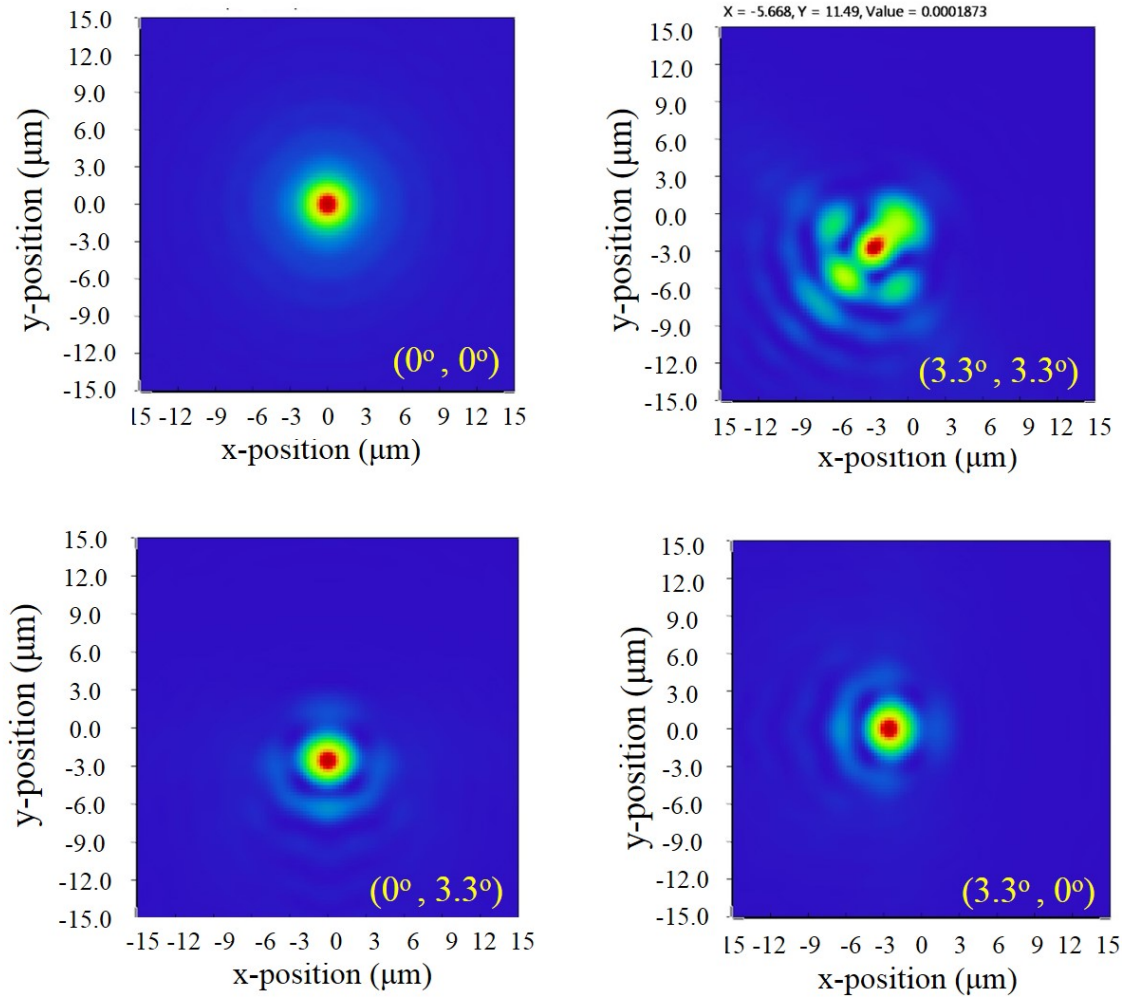
Figure 2-13: Lens system PSF of on-axis and off-axis field angles, acquired through ZEMAX modeling

discussed in Chapter 3. The amount of background noise of the system is determined by the spectral radiance and the bandwith of the filter.

The band-pass filter integrated in the system is a COTS 10-nm FWHM bandpass filter around the beacon center wavelength (850 nm). The filter transmission profile provided from the vendor is shown in Figure 2-14. The filter has a thickness of (5.9 ± 0.1) mm and an optical density (OD) of 4, equivalent to a transmission of 40%. For the current prototype, this filter is integrated in the Matrix Vision camera module through a 3/4-in filter slot.

Image credit: Edmund Optics
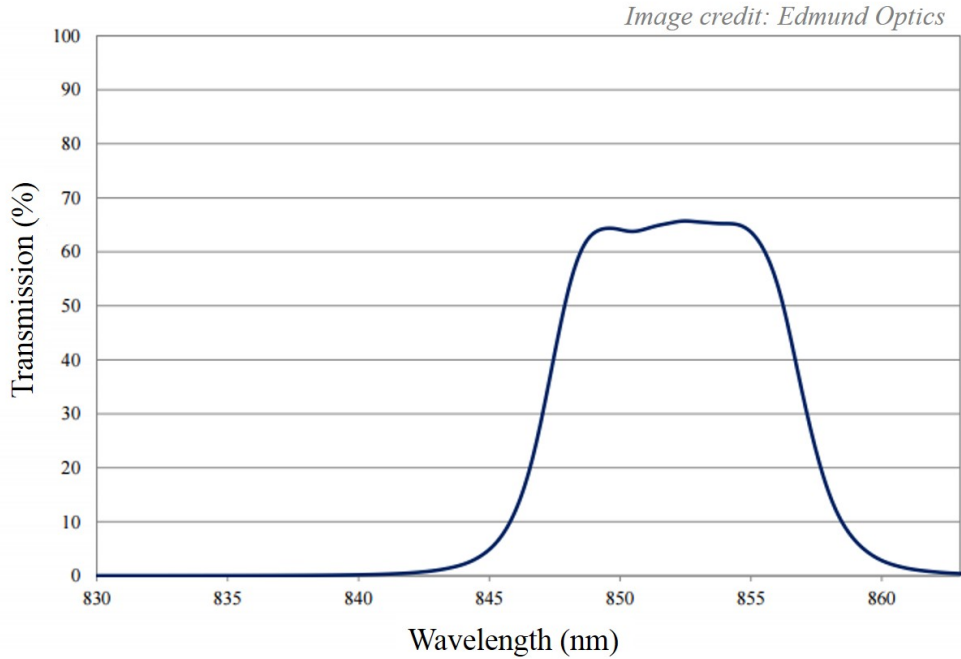
Figure 2-14: Bandpass filter transmission profile, providing a 10-nm window at the beacon wavelength (850 nm) [35]

Long-pass filter   Since the optical elements in the lens system are made of glass that could be damaged by the Sun's UV radiation, a long-pass filter needs to be installed at the lens opening to ensure the lens' integrity for on-orbit operation. The COTS solution selected for the current prototype is the UV/VIS-cut filter from Edmund Optics. The filter is designed to reduce transmission below 720 nm, which covers the UV and visible spectrum. The filter transmission profile is shown in red in Figure 2-15, as provided by the vendor. The filter is approximately 5.9 mm thick with MgF2 coating on both sides.
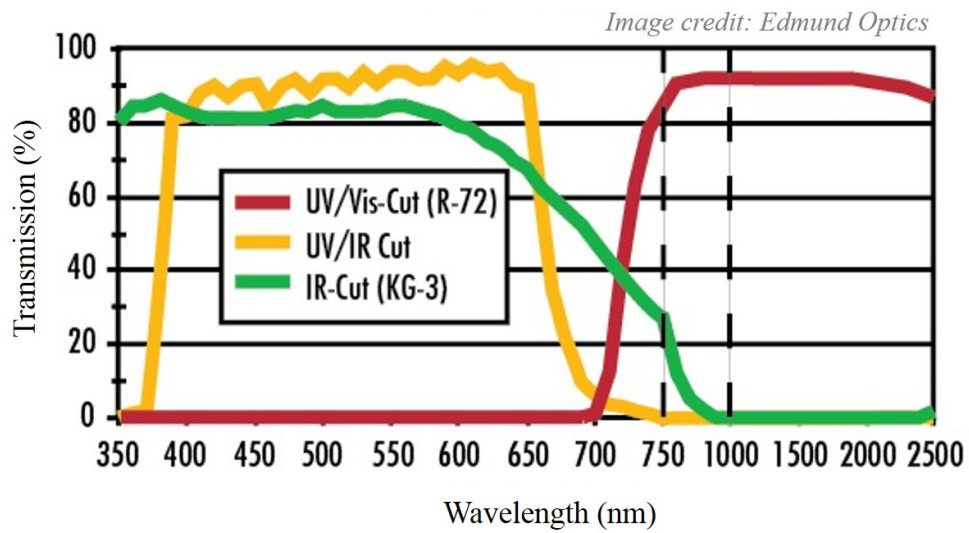
Figure 2-15: UV/VIS-cut filter transmission profile (red), eliminating light below 720 nm in wavelength to reduce UV damage to the system [36]

THIS PAGE INTENTIONALLY LEFT BLANK

Chapter 3

Simulation Development

An end-to-end simulation was constructed in MATLAB to generate the expected beacon image on the detector array. These images will be used to identify the expected attitude accuracy and fade probability of the system through image processing techniques. Figure 3-1 summarizes the simulation structure in a block diagram format.

There are four main models constructed in the simulation: link radiometry model, receiver hardware model, atmospheric turbulence model, and Earth upwelling radiance model. The uplink beacon radiometry module is used to compute the expected optical power density at the spacecraft's receive aperture given the transmitter's properties and orbit configurations. The receiver hardware properties model provides important lens and detector properties such as the point-spread function (PSF), detector's resolution, and noise properties. The atmospheric turbulence model simulates the effect of refractive index inhomogeneity and dynamic wind flow in the atmosphere, causing received power fluctuations. The Earth upwelling radiance under various conditions was inspected to provide the expected background noise level of each frame. All four models were combined in the beacon image generation script, creating the expected image of the beacon beam on the detector array.
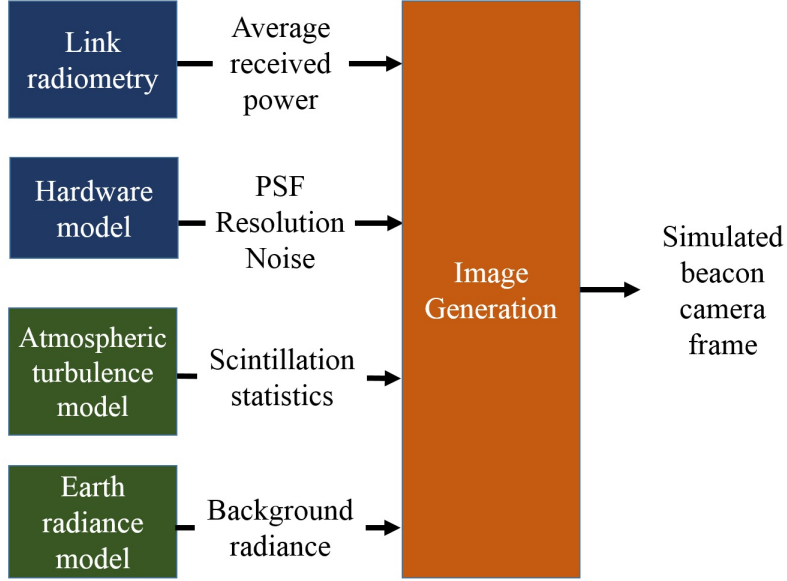
Figure 3-1: Beacon simulation block diagram, consisting of 4 main models: link radiometry, hardware, atmospheric turbulence, and Earth upwelling radiance

3.1 Link Radiometry

The goal of the link radiometry analysis is to compute the average received power through the beacon camera, given the transmitter properties, orbit configuration, channel parameters, and receiver parameters. An illustration of the link configuration along with relevant parameters are shown in Figure 3-2.

Given the transmitter power and beamwidth, the equivalent isotropic radiated power (EIRP) of the transmitter can be computed. The channel losses included in the analysis were free-space path loss, atmospheric absorption and scattering, and optics loss. Free-space path loss increases as the square of the satellite-to-ground range, which can be in the order of 1000 km for a satellite in LEO at low elevation angles. Atmospheric absorption loss is a function of wavelength, sky condition, and elevation angle. The attenuation level at 850 nm for an Earth-space link under clear-sky conditions as a function of elevation angle is shown in Figure 3-3[3]. Optics losses on both transmit and receive platforms can be estimated using existing telescope and camera performance [29]. The link radiometry calculation with transmitter, receiver, and channel parameters can be simplified as shown in Equation 3.1, where P_R, P_T
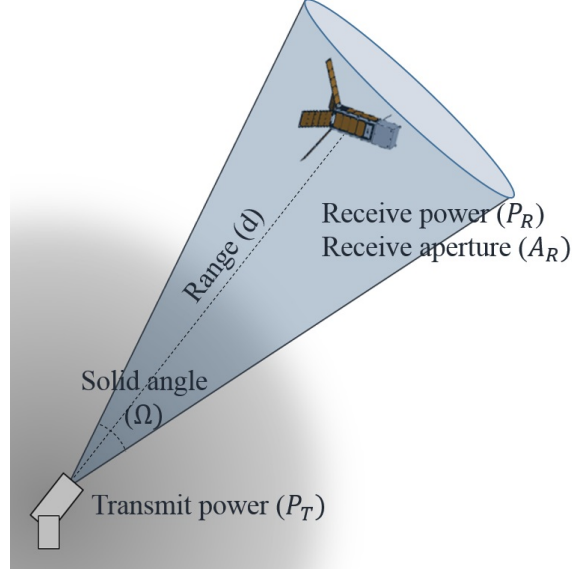
Figure 3-2: Link radiometry configuration, showing the transmitter's, channel's, and receiver's relevant parameters

are the transmit and receive power, respectively, A_R represents the receive aperture area, Ω is the beam solid angle, d is the ground-to-satellite range, L_A, L_O are the atmospheric and optics loss, respectively. The average photon rate received by the detector can be found from the average received power and photon energy at the beacon wavelength. Table 3.1 presents a link radiometry result for a satellite in a 400-km orbit at 20° elevation with baseline transmit power and beam divergence.

$$P_R = P_T \cdot \frac{4\pi}{\Omega} \cdot \frac{1}{4\pi d^2} \cdot \frac{1}{L_A} \cdot \frac{1}{L_O} \cdot A_R \qquad (3.1)$$

3.2   Hardware Model

The optical power received by the aperture is distributed in a point-spread function (PSF) on the focal plane array with size, shape, and resolution defined by the camera hardware properties. The beacon camera components were modeled based on manufacturers' specifications and preliminary hardware testing. The lens system's Zemax model was provided by the vendor, allowing the lens response to be analyzed

Table 3.1: Link radiometry result for a satellite in a 400-km orbit at 20° elevation with baseline transmit power and beam divergence

	Parameters	**Value**	**units**
Orbit parameters	Altitude	400	km
	Elevation angle	20	deg
Transmitter parameters	Transmit power (optical)	10	W
	Wavelength	850	nm
	Beam divergence	5	mrad
	Transmit gain	58	dB
	Transmitter optical losses	-4	dB
Channel parameters	Free-space path loss	-203	dB
	Atmospheric absorption and scattering	-4.5	dB
Receiver parameters	Receive aperture diameter	25	mm
	Receive gain	39.5	dB
	Receive optical loss	-4	dB
	Received power	**-108.3**	**dB**
		$\mathbf{1.5 \times 10^{-11}}$	**W**
	Receive photon flux	$\mathbf{6.4 \times 10^{7}}$	**photons/s**
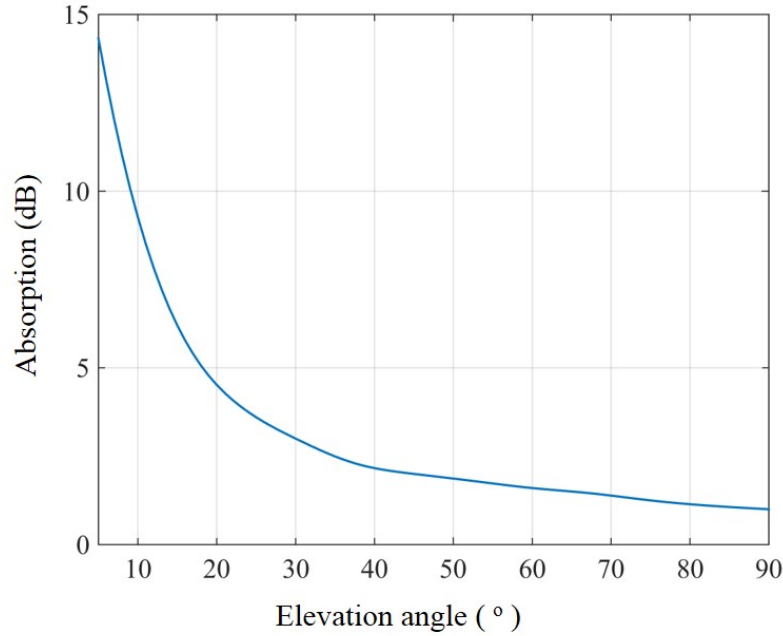
Figure 3-3: Atmospheric absorption level at 850 nm under clear-sky condition as a function of elevation angle [3]

for a variety of field angles. The PSFs in the on-axis and off-axis field angles produced by the Zemax model were shown in Figure 2-13. The PSF images are sampled according to the detector's pixel size to find the expected image of the beacon, as shown in Figure 3-4(a.1) and 3-4(b.1) for the field locations on axis(0°,0°) and at the edge of the FOV (3.3°,3.3°). The brightest pixel flux fraction (BPFF) parameter was used to evaluate the level of focus in each case. The BPFF is defined as the ratio of the photon flux in the brightest pixel to the total photon flux distributed in the PSF. The maximum BPFFs are shown in Figure 3-4(a.2) and 3-4(b.2), corresponding to the on-axis and off-axis case. While there are aberrations in the off-axis case causing PSF distortions, the off-axis BPFF stays relatively close to the on-axis case, ensuring relatively constant signal-to-noise ratio across the field during acquisition. In the tracking mode, the beacon will remain close to the optical axis of the system as the satellite will slew to align itself with the beacon direction. Figure 3-5 shows how the BPFF degrades when the beacon location is displaced in both directions on the detector from the case previously shown in Figure 3-4(a.2). A histogram of the

57

BPFF values are shown in Figure 3-6, showing a normal distribution with a mean value of 9.4% ($\langle B \rangle$) and standard deviation of approximately 1.1% (σ_B), along with a Gaussian fit. The normal probability function estimation of the BPFF distribution is shown in Equation 3.2.
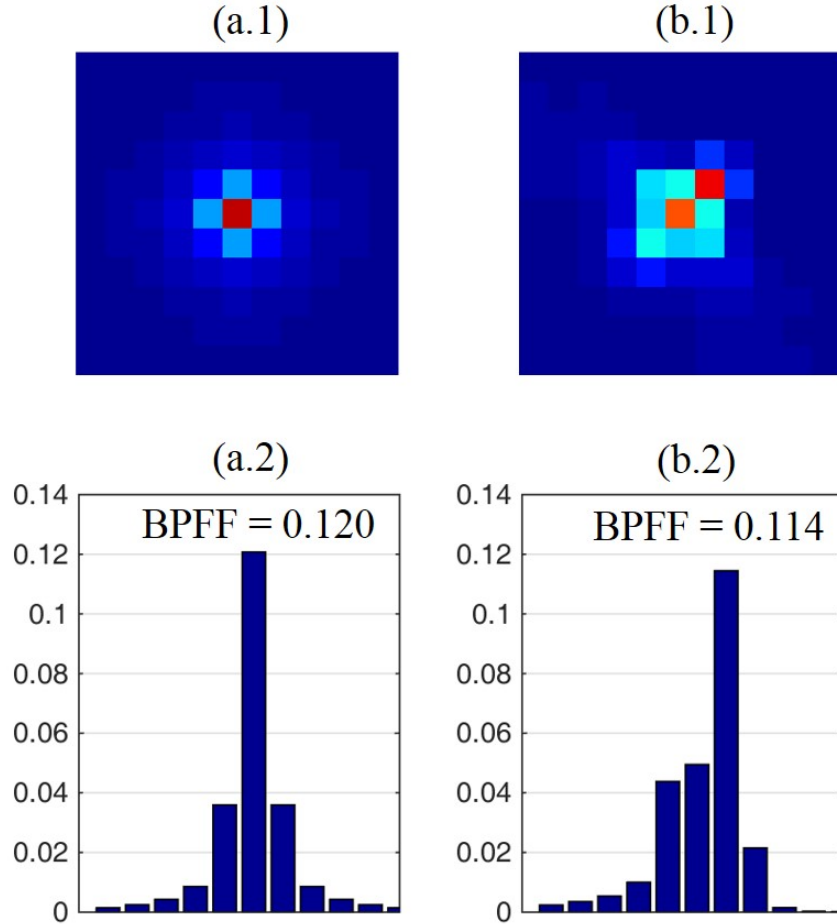
Figure 3-4: (a.1) On-axis PSF as sampled by the detector (a.2) Normalized pixel value of the cross section with the brightest pixel (on-axis) (b.1) Off-axis PSF as sampled by the detector (b.2) Normalized pixel value of the cross section with the brightest pixel (off-axis)

$$f_{BPFF}(B) = \frac{1}{\sigma_B \sqrt{2\pi}} e^{-\frac{(B - \langle B \rangle)^2}{2\sigma_B^2}} \tag{3.2}$$

The optical power on the detector was converted to a number of electrons based on the photon power at the wavelength of interest and the detector's quantum efficiency (QE). The charge on each pixel was further adjusted to include detector's
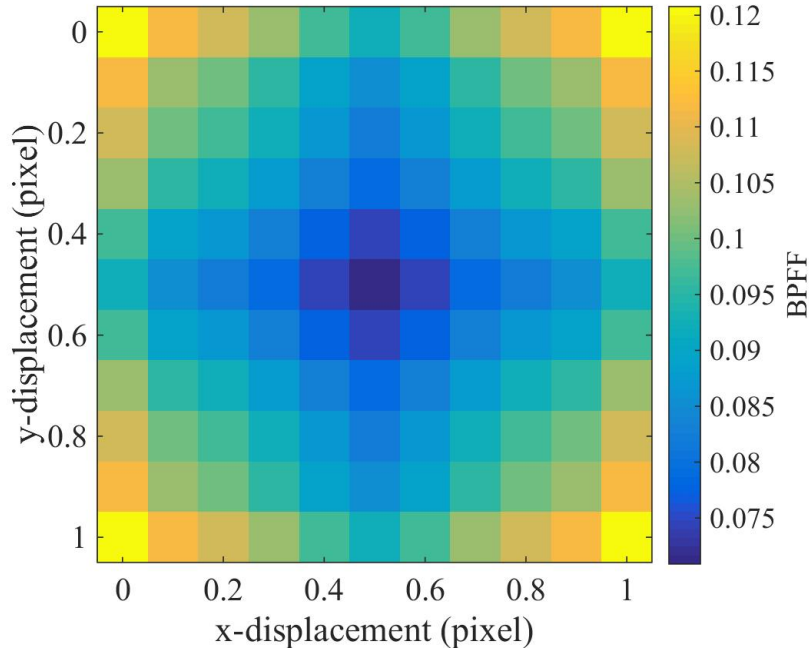
Figure 3-5: BPFF map for the on-axis case as a function of centroid displacement relative to the center of a pixel.

noise parameters. Read noise was modeled as a Gaussian random parameter with the root-mean square value provided in the detector's data sheet. Dark current noise was modeled as a Poisson distribution with the mean at the average dark current value provided by the manufacturer. Multiple dark frames were taken with the camera prototype to investigate the number of bright damaged pixels. The result shows that there are less than 10 permanently bright pixels with the brightest pixel at 0.8% well capacity, which is currently modeled in the simulation. More pixels are expected to be damaged by radiation, which can be easily adjusted in the simulation. Image processing techniques will be developed to mitigate the effects of these damaged pixels.

3.3   Atmospheric Turbulence Model

The uplink beacon propagates through Earth's turbulent and inhomogeneous atmosphere, causing random irradiance fluctuations at the receiver's end, referred to as
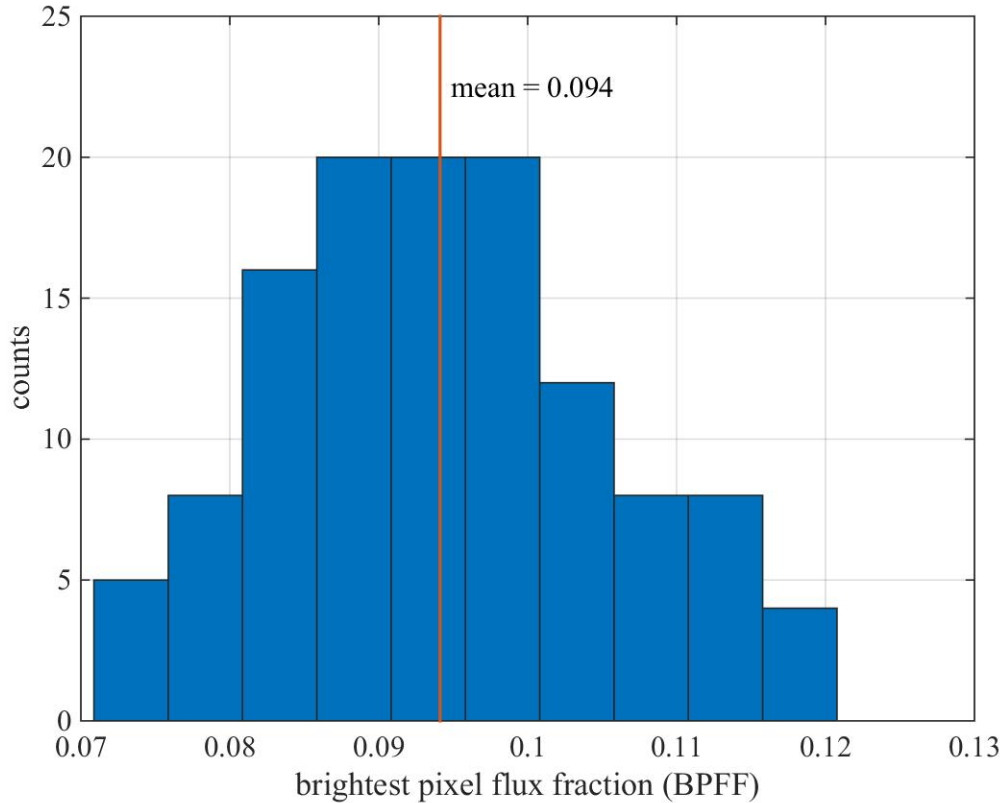
Figure 3-6: Histogram of BPFF distribution, showing a Gaussian behavior with $\mu = 0.094$ and $\sigma = 0.011$

scintillation. The effect of scintillation on the uplink path is more drastic than the downlink path due to the beam being distorted early on its path in the atmosphere before propagating in free space. For this reason, the satellite aperture always lies within the same atmospheric coherence zone, causing the entire received image to fade or surge corresponding to the turbulence dynamic. [37] Scintillation depends greatly on the atmospheric turbulence strength, which can be quantified by the refractive index structure parameter (C_n^2). C_n^2 varies according to several parameters such as geographical location, weather conditions, and time of day. One of the most commonly used C_n^2 parametric models for daytime conditions is the Hufnagel-Valley model, shown in Equation 3.3.[1, 38]

$$C_n^2(h) = 0.00594 \left(\frac{w}{27}\right)^2 (10^{-5}h)^{10} e^{-h/1000} + 2.7 \times 10^{-16} e^{-h/1500} + Ae^{-h/100} \qquad (3.3)$$

where h represents altitude measured in m, w is the root-mean-square wind speed in m/s, and A is the nominal value of $C_n^2(0)$ at ground level in $m^{-2/3}$. The rms wind speed w can be found as a function of the ground wind speed V_g and slew rate ω_s, as shown in Equation 3.4 and 3.5.[38] For a satellite in LEO moving with respect to an observer on the ground, the corresponding slew rate can get up to $1°/s$, a dominant contribution to the wind speed value at high altitude. The C_n^2 profiles for a stationary beam and a beam with $1°$ slew speed are shown in Figure 3-7.

$$w = \left(\frac{1}{15 \times 10^3} \int_{5\times10^3}^{20\times10^3} V^2(h)dh \right)^{1/2} \qquad (3.4)$$

$$V(h) = \omega_s h + V_g + 30 \exp\left(\frac{h - 9400}{4800}\right)^2 \qquad (3.5)$$

With the C_n^2 profile of the atmosphere, the scintillation index of a laser beam along the uplink channel can be determined following the strong fluctuation theory [38]. The scintillation index σ_I^2 can be derived as shown in Equation 3.6 - 3.8, where H is the satellite altitude, k is the wavenumber of the beam, and ζ is the off-zenith angle.[38] To reduce the effect of scintillation, spatial diversity is often used where multiple transmit lasers are mounted in different coherence zones. Since each beam propagation process can be treated as statistically independent, the scintillation index can be scaled down with the number of independent beams. Figure 3-8 shows the scintillation index as a function of elevation angle for a transmitter with 4 independent beams for spatial diversity to a satellite in a 400-km orbit. As a general trend, the scintillation index increases with elevation angle due to increasing slew speed and approaches a constant level due to the asymptotic behavior of the strong fluctuation theory.

$$\sigma_I^2 = \exp \frac{0.49\sigma_{Bu}^2}{(1 + 1.12\sigma_{Bu}^{12/5})^{7/6}} + \frac{0.51\sigma_{Bu}^2}{(1 + 0.69\sigma_{Bu}^{12/5})^{5/6}} - 1 \qquad (3.6)$$
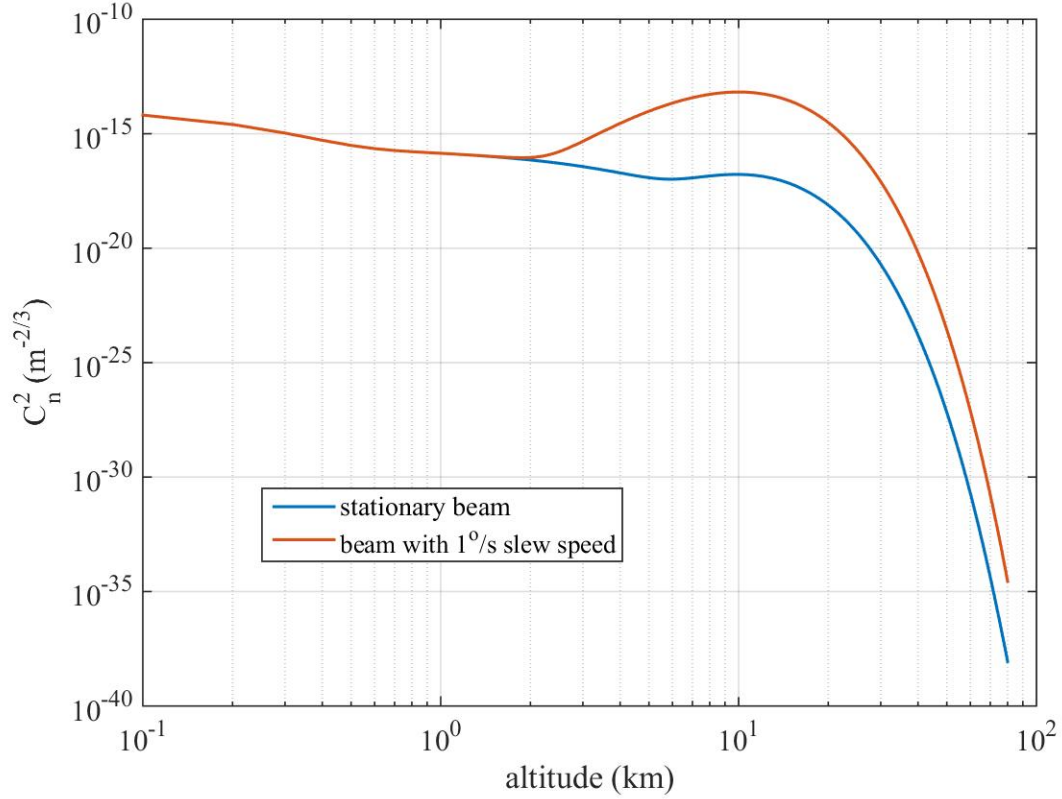
Figure 3-7: C_n^2 profiles following the Hufnagel-Valley model for a stationary beam and a beam with $1°$ slew speed

$$\sigma_{Bu}^2 = 8.70\mu_{3u}k^{7/6}H^{5/6}\sec^{11/6}\zeta \tag{3.7}$$

$$\mu_{3u} = Re\left(\int_0^H C_n^2(h)\left(\xi^{5/6}(i(1-\xi))^{5/6}\right)dh\right)$$

$$\text{where } \xi = 1 - \frac{h}{H} \tag{3.8}$$

The scintillation statistics can be described with a log-normal distribution, where the variance equals the previously computed scintillation index σ_I^2. The power at the receive aperture fluctuates according to this log-normal distribution, as shown in Equation 3.9, where $p_I(I)$ represents the probability that the signal brightness equals to I and $\langle I \rangle$ is the average power received as computed in the link radiometry analysis. Figure 3-9 shows the probability density functions (PDF) for various values
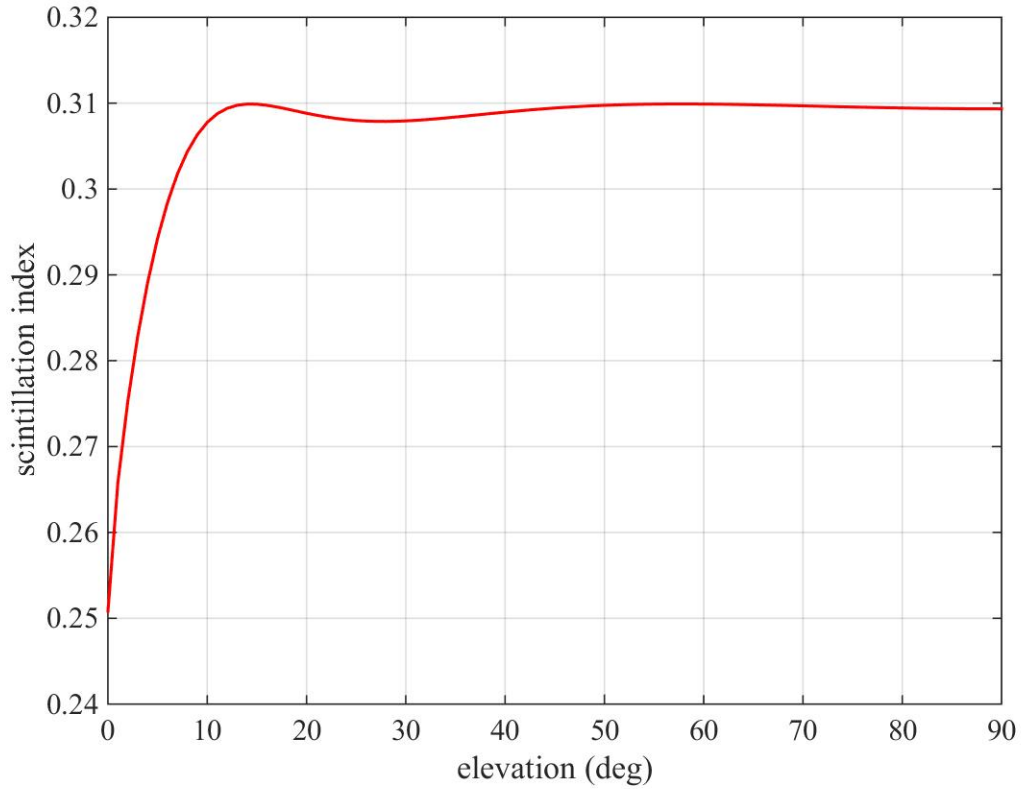
Figure 3-8: Scintillation index as a function of elevation angle for a 4-beam transmitter and satellite in a 400-km orbit

of scintillation indices. It can be seen that high scintillation index leads to high probability of fades and occasional surges in the received power.

$$f_I(I) = \frac{1}{\sqrt{2\pi} I \sigma_I} \exp - \frac{\left(\ln \left(\frac{I}{\langle I \rangle} \right) + \frac{1}{2} \sigma_I^2 \right)^2}{2 \sigma_I^2} \tag{3.9}$$

3.4   Earth Upwelling radiance

While the other models in the simulation are concerned with the beacon signal received at the satellite terminal, beacon detection analysis also requires extensive knowledge of the background noise level during operation. To assess the background radiance level at 850 nm, data from the Landsat-8 mission was queried for multi-
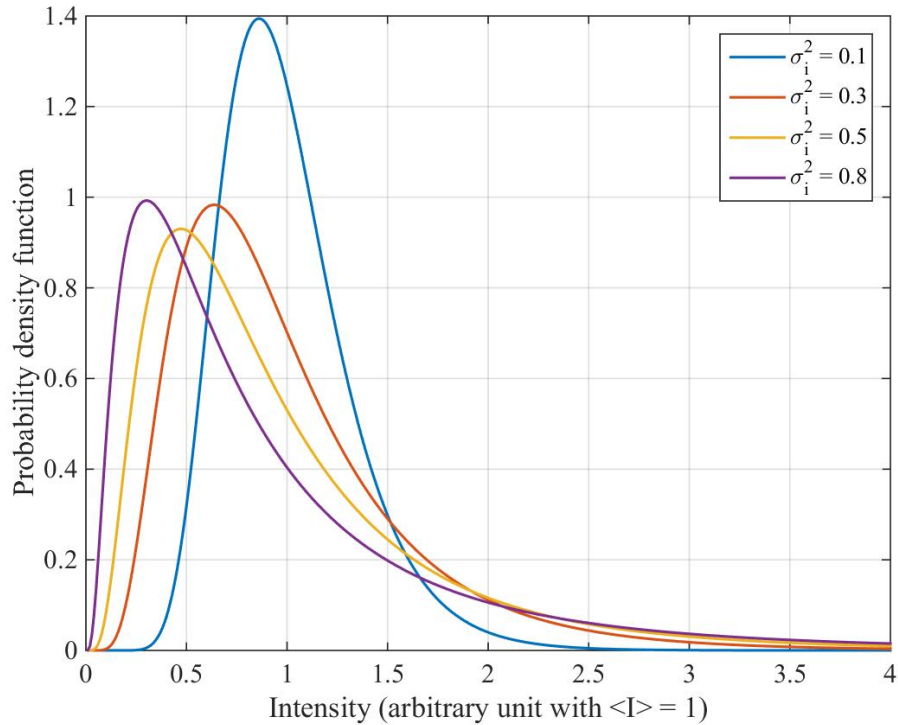
Figure 3-9: Log-normal probability density function with various values. Higher scintillation index indicates higher variance in the intensity PDF, leading for wider range of intensity fluctuations and higher fade probability, which can be visualized as the area under the curve for I < 1

ple cloud coverage conditions at various cities in the United States during daytime. Landsat-8 is the most recent spacecraft in the Landsat series, a collaboration between NASA and US Geological Survey (USGS) with the goal of providing continuous global images in a number of spectral bands of scientific interests. The Landsat-8 spacecraft was launched in 2013 and is currently in a 705-km altitude circular polar orbit. The Landsat 8 spacecraft carries two sensors, the Operational Land Imager (OLI) and the Thermal Infrared Sensor (TIRS), collecting over 500 images per day. The spectral bands covered by the OLI and TIRS instrument on LandSat 8 are shown in Figure 3-10. The OLI's spectral band consists of a NIR band (band 5) covering the range of 0.85 μm to 0.88 μm, coinciding with the selected beacon wavelength.[39] Since Landsat-8 level 1 data products are publicly available in the USGS archives with no restrictions, images in band 5 were queried and downloaded from the archive

64

for further analysis. Examples of the images acquired from the database are shown in Figure 3-11 for the Boston region under four different cloud coverage conditions in the NIR band.[40]
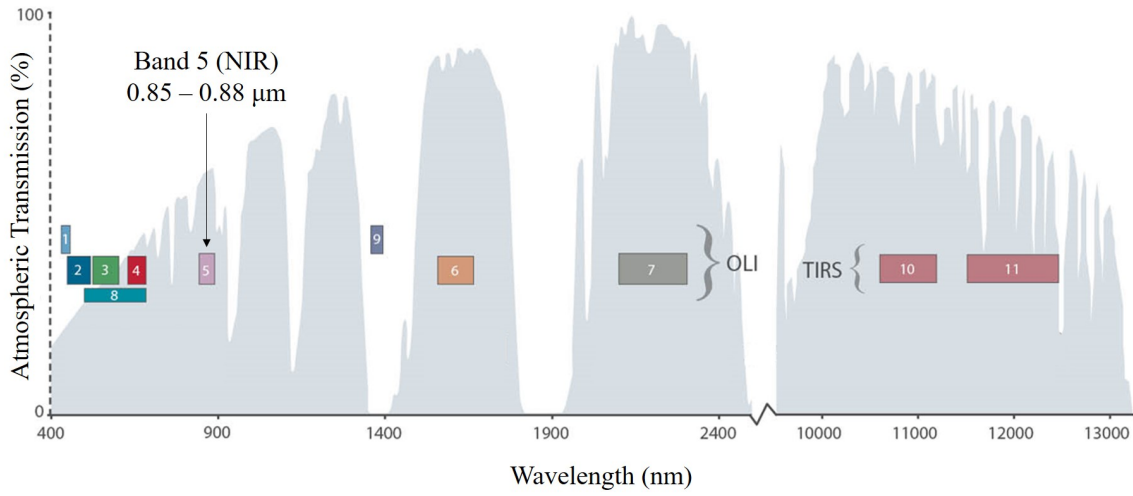
Figure 3-10: LandSat 8 OLI and TIRS spectral bands

Each Landsat-8 OLI image downloaded is accompanied by a data file that contains radiometric calibration coefficients that can be used to convert image digital numbers (DN) to spectral radiance values of the scene at the sensor aperture. The calibration method is summarized in Equation 3.10.[41, 42]

$$L_\lambda = G_{rescale} \times Q_{cal} + B_{rescale} \qquad (3.10)$$

where:

L_λ: spectral radiance $[W/(m^2 sr\mu m)]$

Q_{cal}: quantized calibrated pixel value $[DN]$

$G_{rescale}$: band-specific rescaling gain factor $[W/(m^2 sr\mu m)/DN]$

$B_{rescale}$: band-specific rescaling bias factor $[W/(m^2 sr\mu m)]$

Landsat 8 images in band 5 from Boston, Los Angeles, Seattle, and Houston were downloaded from the USGS server with 20 images per city for a variety of weather conditions during day time. The average brightness of each scene was first

65
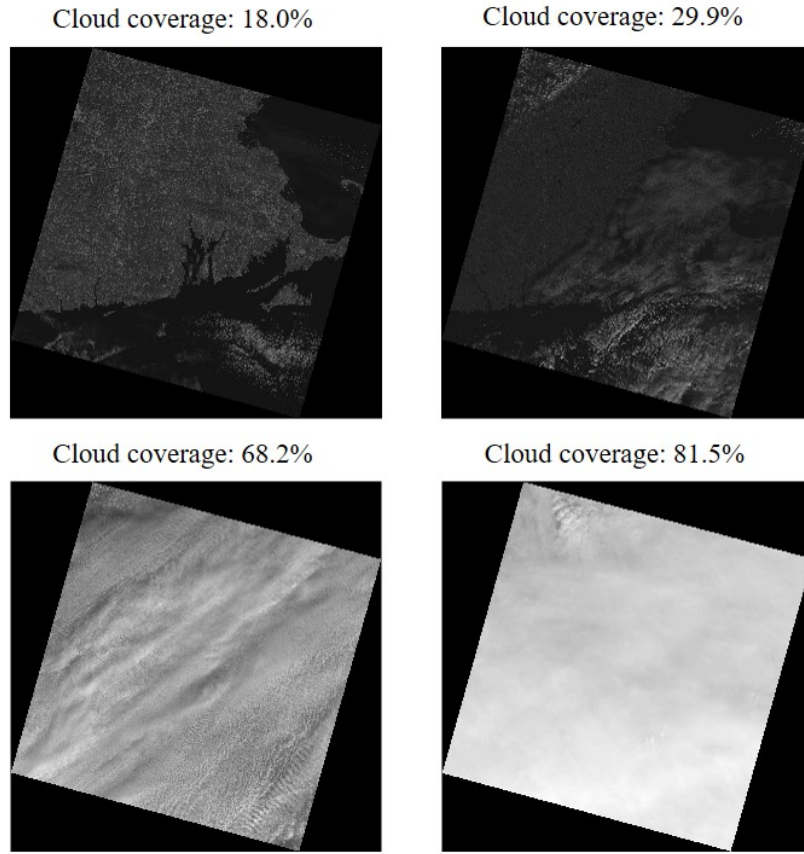
Figure 3-11: Landsat 8 OLI band 5 images of the Boston region under various cloud coverage conditions. Higher cloud coverage percentage leads to higher spectral radiance due to clouds' albedo.

computed in DN, then converted to a corresponding average spectral radiance based on calibration coefficients and formula shown in Equation 3.10. The average spectral radiance results are shown in Figure 3-12 as a function of cloud coverage and sun elevation angle. Figure 3-13 shows a statistical summary of all 80 average spectral radiance values in box plot format. The minimum, maximum, and median values, as marked, are used as representative background radiance scenarios in the simulation. The maximum spectral radiance value 188 W/m^2/sr/μm is in agreement with previous findings on Earth's upwelling radiance in sunlit cloud condition at 850 nm.[3]
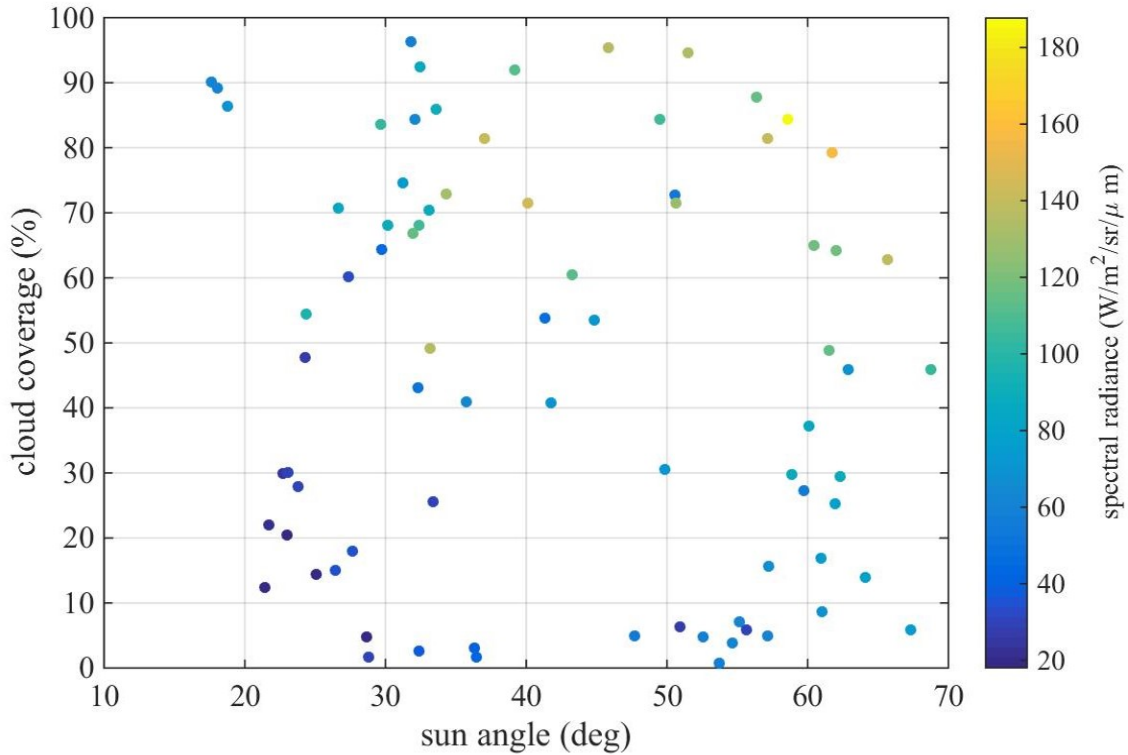
Figure 3-12: Average spectral radiance of 80 LandSat-8 images from Boston, Los Angeles, Seattle, and Houston as downloaded from the USGS server. The results are shown as a function of cloud coverage and sun angle. High background spectral radiance causes low signal-to-noise ratio, degrading the beacon tracking performance.

3.5 Beacon Image Generation

After the model development process, simulated camera frames can be generated for various orbit configurations and weather conditions. The beacon frames are constructed by overlaying the image of the beacon's PSF on a background frame, with average brightness determined in the background radiance analysis. The average beacon brightness is determined in the link radiometry model, with intensity fluctuations following the atmospheric scintillation log-normal statistics, as described in the atmospheric turbulence model. The background frame was constructed pixel-by-pixel, where each pixel value follows a Poisson distribution with the mean value computed
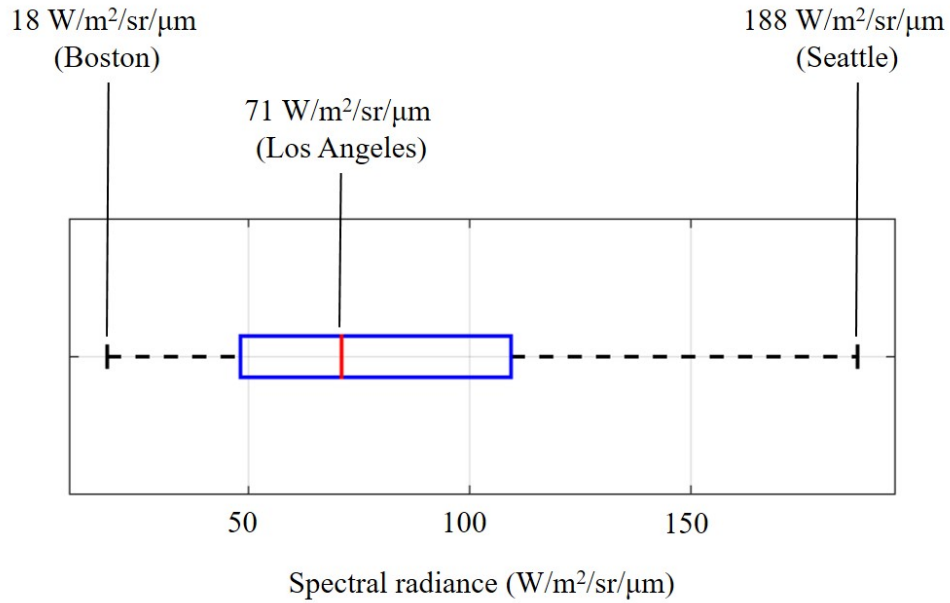
Figure 3-13: Statistical summary of average spectral radiance of LandSat-8 images, showing the minimum, median, and maximum values

from the Earth radiance model. Detector's noise and signal's shot noise are also included in the frame generation process. The camera integration time is set such that the maximum total number of electrons generated from both signal and noise sources in a pixel reaches 50% of detector's full-well capacity. As a result, the integration time is shorter in bright background conditions than in low-light conditions. Figure 3-14 shows simulated camera frames for a satellite at 20° elevation angle under 3 background spectral radiance conditions as specified in Figure 3-13 (18, 71, 188 $W/m^2/sr/\mu m$). The color scale is shown in number of electrons generated in each pixel.

3.6   Acquisition and Tracking algorithms

Beacon acquisition and tracking algorithms were developed to extract attitude knowledge through beacon frame image processing, emulating the function of on-board flight software. The acquisition and tracking process is initiated through radio command at the beginning of each pass after the satellite has established relative coarse
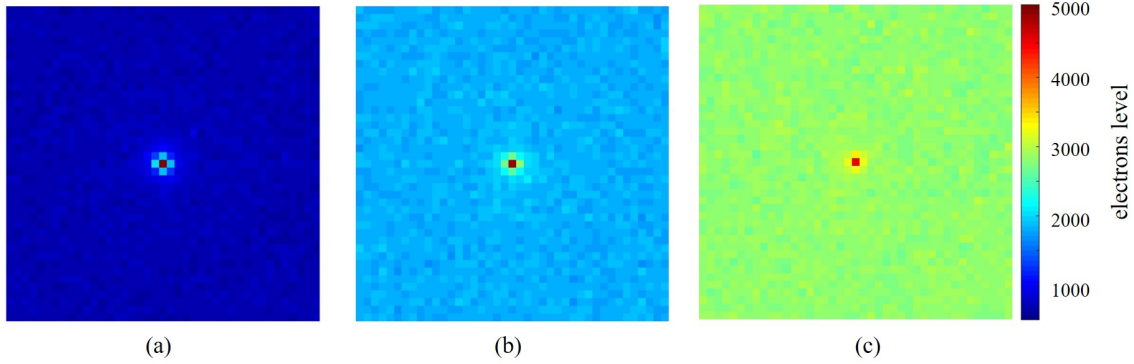
Figure 3-14: Simulated camera frames at 20° elevation angle at 3 background radiance levels: (a) 18 W/m²/sr/μm (min), (b) 71 W/m²/sr/μm (median), (c) 188 W/m²/sr/μm (max)

pointing at the ground station such that the laser beacon is expected to be within the camera's field-of-view. The process is terminated through radio command at the end of each pass. The acquisition algorithm is used for beacon searching at the beginning of a pass or when the beacon was lost due to weather or other interruptions. The tracking algorithm was developed to follow the beacon signal efficiently and reliably once it has been acquired. The baseline acquisition and tracking flow chart is shown in Figure 3-15.

The acquisition process begins with the flight software reading out full-frame images from the beacon camera from which it determines the brightest pixel. To reduce the probability of false detection, the pixel value of the brightest pixel is compared with a detection threshold value, pre-computed using expected beacon radiance at the satellite terminal. In flight software implementation, this parameter will be tunable via radio uplink for re-configuration flexibility. To further ensure that the beacon is correctly acquired, a brightest pixel location consistency check is implemented. Since the satellite's dynamic is slower than the camera's frame rate, the beacon image, if acquired, will follow a predictable pattern. When the brightest pixel location becomes erratic, it is an indication that various background pixels are brighter than the beacon pixel. This check can be implemented by finding the locations of the brightest pixel in the multiple consecutive frames and compare their relative positions. When

69

Acquisition
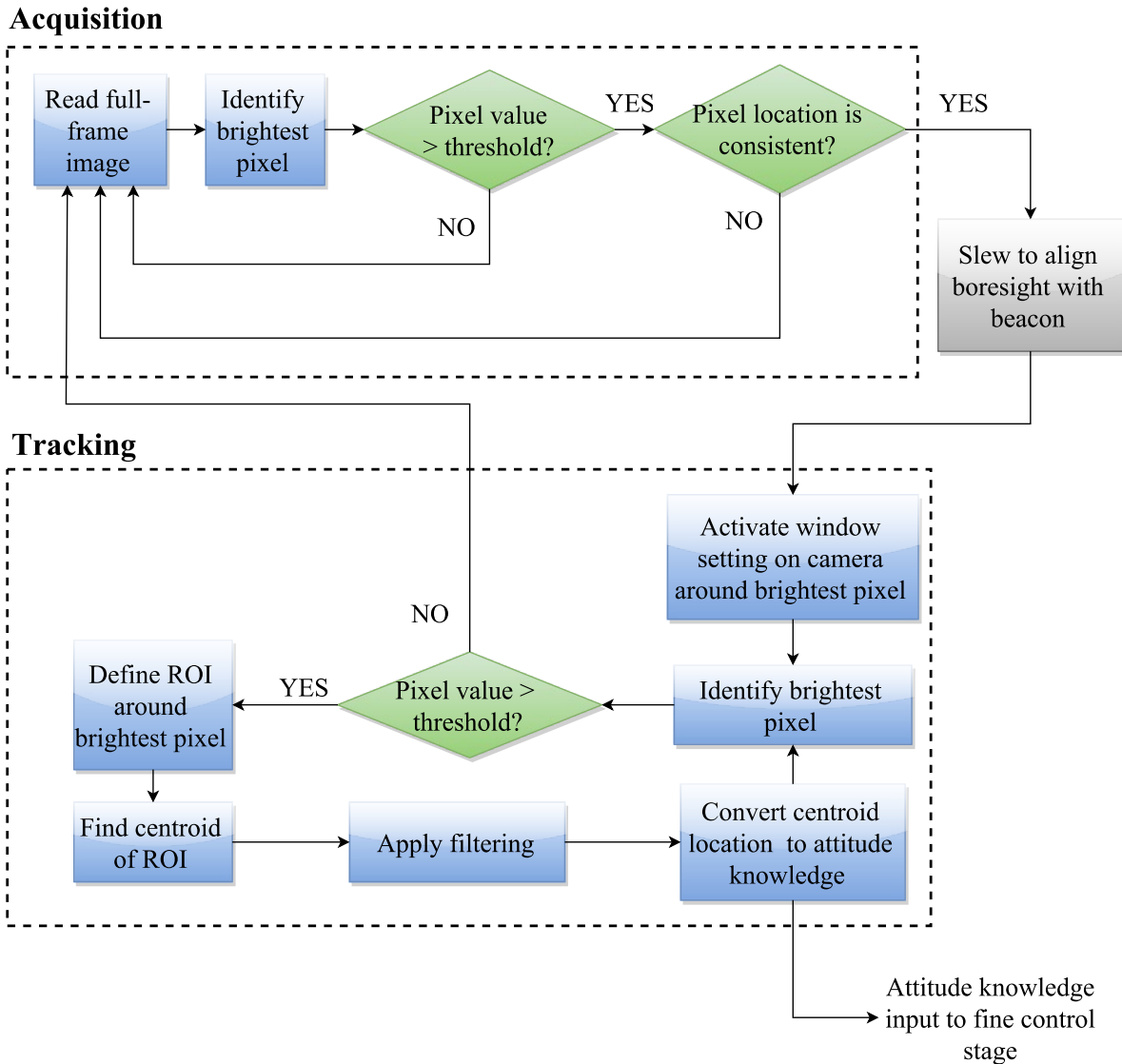
Tracking

Figure 3-15: Baseline acquisition and tracking flow chart, showing the acquisition and tracking transition before the computation of attitude knowledge

the location variations stay within a predefined limit, the flight software can declare beacon acquisition. At this point, the satellite will slew toward the beacon direction using coarse actuators, driving the beacon image toward the center of the detector array.

In tracking mode, the "windowing" setting of the CMOS camera is utilized to increase frame rate and reduce probability of false detection. The window is defined around the brightest pixel location of the previous frame and has a size determined by

the expected spacecraft dynamics. The brightest pixel within the window is identified and compared with a threshold value to ensure the beacon has not faded or moved outside of the window frame. If the brightest pixel value is less than the threshold value during tracking mode, the beacon is declared lost and the acquisition process will be re-activated. If the brightest pixel value exceeds the threshold value, the tracking algorithm proceeds to find the centroid location within the region-of-interest (ROI), which is defined by the lens system's point-spread function (PSF) size. The center-of-mass (COM) centroiding method is used on the ROI pixels to compute the beacon location on the detector. The centroiding method is shown in Equation 3.11 and illustrated in Figure 3-16, where $f(x_i, y_i)$ denotes the pixel value at location (x_i, y_i) and N represents the ROI size in number of pixels. Estimation techniques such as Kalman filtering are employed to improve the beacon location estimation, especially under extreme background noise conditions. Lastly, the location of the beacon image on the detector can be converted into an angular boresight offset that can be corrected by the fast-steering mirror (FSM) in the fine control stage, as shown in Equation 3.12, where x_c, y_c represent the centroid location, x_0, y_0 represent the center of the detector or boresight location, and f is the lens system effective focal length.

$$
\begin{aligned}
x_c &= \frac{\sum_{i=1}^{N} \sum_{j=1}^{N} x_i f(x_i, y_i)}{\sum_{i=1}^{N} \sum_{j=1}^{N} f(x_i, y_i)} \\
y_c &= \frac{\sum_{i=1}^{N} \sum_{j=1}^{N} y_i f(x_i, y_i)}{\sum_{i=1}^{N} \sum_{j=1}^{N} f(x_i, y_i)}
\end{aligned}
\tag{3.11}
$$

$$
\begin{aligned}
\theta_x &= \frac{x_c - x_0}{f} \\
\theta_y &= \frac{x_c - x_0}{f}
\end{aligned}
\tag{3.12}
$$
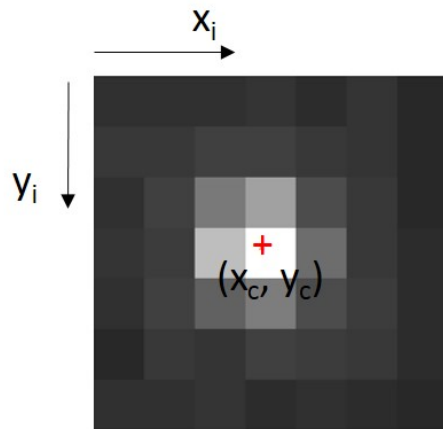
Figure 3-16: Illustration of center-of-mass centroiding method

Chapter 4

Simulation Results

4.1 Figures of Merit

The goal of the simulation is to assess the system's performance during tracking mode quantitatively through two main figures of merit: detection probability and attitude accuracy. The detection probability is defined as the probability that the brightest pixel in the camera frame belongs to the beacon image assuming there is no obstruction in the line-of-sight, which can be estimated through analytic beacon and background statistics or through a Monte-Carlo simulation. The attitude accuracy is defined as the angular error between the actual beacon direction and the estimated beacon direction through centroiding of the beacon image on the detector in the presence of background noise and detector's noise.

The detection probability can be estimated analytically through a signal-to-brightest-noise ratio (S/N_b), which is defined as the ratio between the primary beacon pixel and the brightest background pixel. Detection is considered to be successful when $S/N_b > 1$. The denominator N_b represents the brightest background pixel, which can be found through the assumption that the background noise follows a Poisson distribution and that all pixels are uncorrelated.The primary beacon pixel can be computed as the product of the power received with scintillation statistics and the brightness probability of the brightest pixel. The average signal-to-brightest-noise ratio $\langle S/N_b \rangle$ can be computed using the average power received from link radiometry analysis and

the average brightest pixel flux fraction of the system, as shown in Equation 4.1. The average power received by the camera aperture can be computed as shown in the link radiometry analysis as a function of orbit configuration, transmitter, and channel parameters. The average BPFF was shown in the hardware model section to be approximately 9.4% for the on-axis case.

$$\langle S/N_b \rangle = \frac{\langle I \rangle \cdot \langle B \rangle}{\sqrt{2} \cdot \mathrm{erf}^{-1}(1 - \frac{1}{N}) \cdot \sigma_b} \tag{4.1}$$

where:

$\langle S/N_b \rangle$: average signal-to-brightest-noise ratio

$\langle I \rangle$: average photon flux received by the camera aperture

$\langle B \rangle$: average brightest pixel flux fraction

N: number of pixels in the focal plane array

σ_b: variance of background Poisson noise distribution

The fade probability can be computed by finding the probability that S/N_b is less than 1, where the probability density function of S is the product of the log-normal scintillation probability and the normal BPFF probability density function, as shown in Equation 4.2. The scintillation probability was shown in Equation 3.9 and the BPFF probability function is shown in Equation 3.2. Equation 4.2 an be solved numerically for a variety of orbit configurations and background radiance.

$$\begin{aligned} P_{fade} &= P(I \cdot B < N_b) \\ &= \iint_{I \cdot B < N_b} f_{scin}(I) f_{BPFF}(B) \, dI \, dB \\ &= \int_{-\infty}^{\infty} f_{scin}(I) F_{BPFF}\left(\frac{N_b}{I}\right) dI \end{aligned} \tag{4.2}$$

where:

f_{scin}: scintillation probability density function

f_{BPFF}: BPFF probability density function

F_{BPFF}: BPFF cumulative distribution function

N_b: brightest background pixel

A Monte-Carlo simulation was also created for attitude accuracy estimation and secondary fade probability analysis. The simulation was created with scintillation statistics of the beacon brightness, Poisson statistics of the background pixels, and the random walk behavior of the beacon location. Beacon image generation as described in Chapter 3 were implemented for 200 consecutive frames. The number of frames where the beacon brightest pixel flux is less than the brightest background flux were counted and the fade percentage was computed. The attitude accuracy can be computed by region-of-interest reduction and centroiding algorithm as described in Chapter 3.

4.2 Detection Probability

The detection probability can be visualized through average S/N_b analysis. Although this analysis does not include scintillation statistics and BPFF distribution, it can provide a qualitative estimate of the beacon brightness compared to background noise level. Figure 4-1 shows the average S/N_b values in dB for 3 representative sky spectral radiance scenarios as shown in Chapter 3 over a range of elevation angles. The $\langle S/N_b \rangle$ increases with elevation angle due to shorter path length, which leads to lower free-space path loss as well as atmospheric absorption. Lower background spectral radiance reduces the noise level and leads to higher $\langle S/N_b \rangle$. A high $\langle S/N_b \rangle$ indicates that there is high probability that the beacon can be detected while low $\langle S/N_b \rangle$ indicates high probability of fading. In the highest background radiance case, it is not likely that the beacon can be found with reasonable fidelity below 10° elevation angle. In all sky spectral radiance scenarios, it is likely that the beacon can be found with high probability above 20° as there is a margin of at least 6 dB in all cases.

The fade probability can be found analytically via Equation 4.2 to yield quantitative results. Figure 4-2 shows the fade probability in log scale for the extreme and median spectral sky radiance values for elevation angles from 5° to 45°. The results
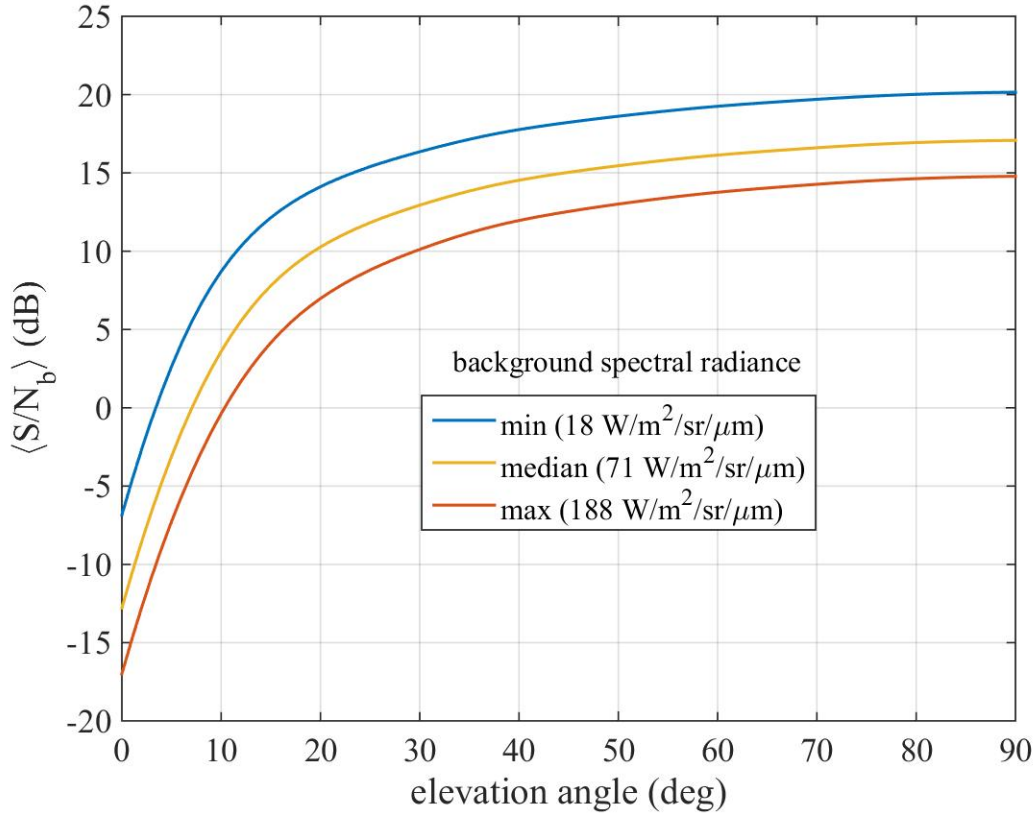
Figure 4-1: Average S/N_b values for 3 representative sky brightness conditions as a function of elevation angle. $\langle S/N_b \rangle$ is high for low background spectral sky radiance and low for high spectral sky radiance. $\langle S/N_b \rangle$ increases with elevation angle due to shorter path length.

show that above 20° elevation, the fade probability in all cases is below 1%, yielding a reliable detection probability when there is no obstruction directly in the line of sight. Fade probability of less than 1% can be achieved at 14° for the median spectral sky radiance case and at 8° in the darkest sky condition. Detection probability of > 90% can be achieved in all sky conditions above 15° elevation angle.

The Monte-Carlo simulation results provides a secondary fade probability estimation that can be used to validate the analytical method. Figure 4-3 shows a time series of the actual S/N_b value results in dB from the Monte-Carlo simulation for a satellite at 15° elevation angle under brightest sky conditions. A fade event occurs when the beacon pixel is not the brightest pixel or, equivalently, when S/N_b is less than 0 dB.

76
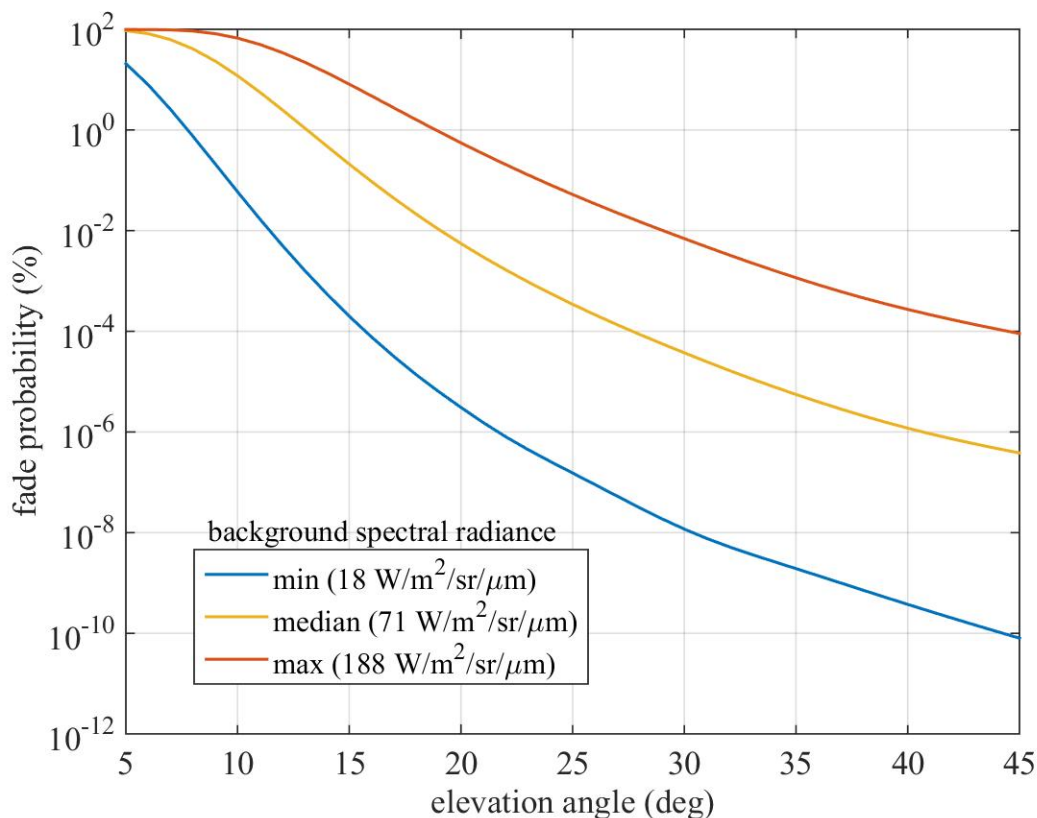
Figure 4-2: Analytical fade probability estimation for 3 representative sky brightness conditions as a function of elevation angle, computed through integration of the scintillation and BPFF statistics, as shown in Equation 4.2

The Monte-Carlo and analytical estimation results are shown in Figure 4-4 for 3 sky conditions at 5° to 25°. The Monte-Carlo approach does not have the sensitivity to estimate the fade probability beyond 25° elevation angle due to limited frames generated. The Monte-Carlo simulation results agree with the previous analytical estimation in all cases, showing credibility in the fade probability calculation results. The root-mean-square difference of the two fade probability calculation methods is within 3% for all cases, with better agreement at low sky radiance. The fade probability can be reduced through estimation method, which is not within the scope of this document, to provide more reliable results.
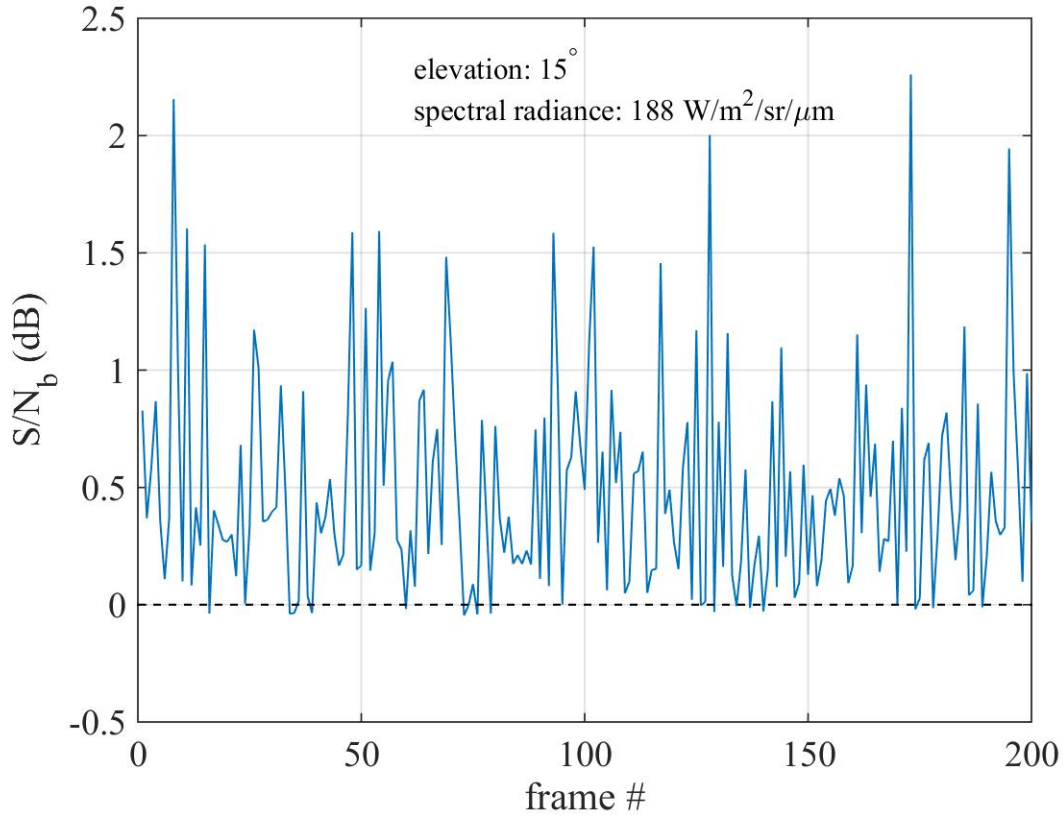
Figure 4-3: S/N_b values at brightest background condition at 15° elevation angle for 200 continuous frames

4.3 Attitude Accuracy

The attitude accuracy was computed by comparing the estimated beacon location through centroiding and the true beacon location input. The analysis is applied for all sky conditions above 15° elevation, where fade conditions are less than 10% and can be corrected through basic estimation methods for continuous beacon detection. Figure 4-5 shows the estimated centroid location and the true centroid location on the detector for the minimum spectral sky condition at 15° elevation angle. The residual between the estimated and true beacon location in pixels was computed and converted into angular error measurement following Equation 3.12.

Figures 4-6 shows the attitude accuracy when the beacon is found as a function of elevation angle for the minimum, median, and maximum background sky condition, respectively. The attitude knowledge accuracy in all cases is less than 0.08 mrad,
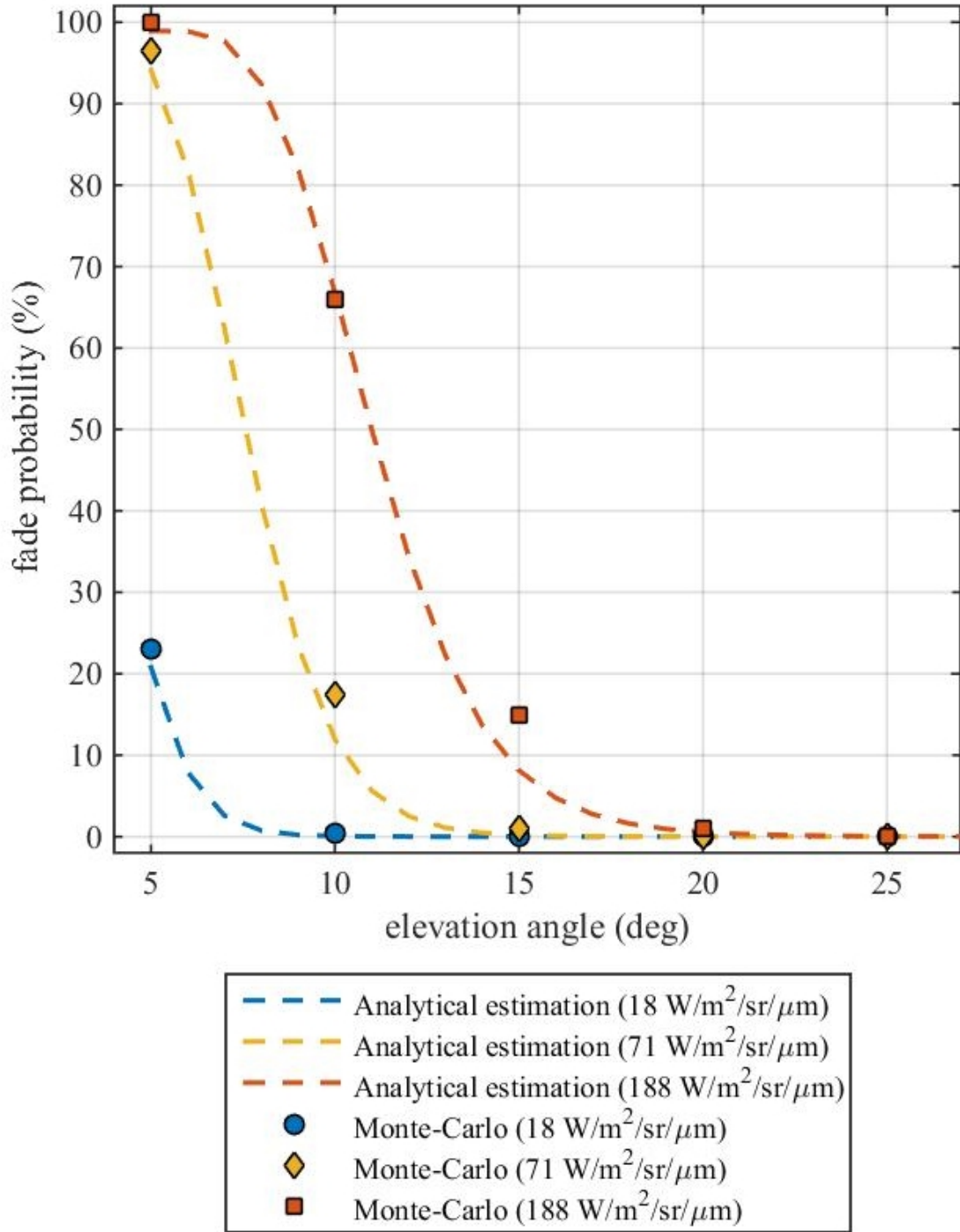
Figure 4-4: Monte-Carlo fade probability results in comparison with analytical estimates. Both methods agree to within 3% in all cases with lower residual at low sky radiance.

which contributes to less than $\frac{1}{10}$ of the pointing budget, specified at 1.05 mrad. The average attitude accuracy is approximately 20 μrad, resulting from a 0.3 pixel average
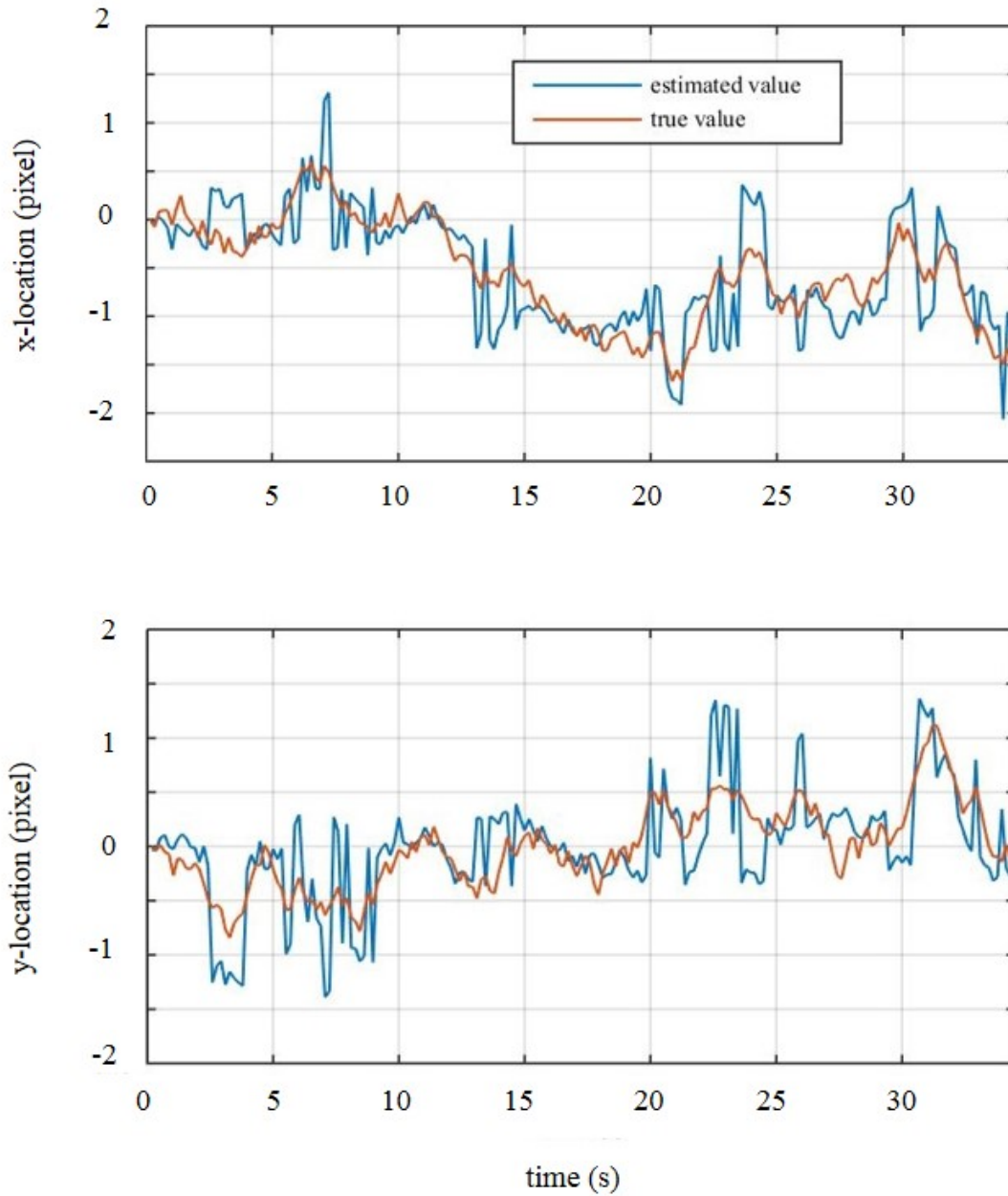
Figure 4-5: Time series of estimated centroid location and true beacon location at minimum sky brightness conditions at 15°elevation angle

centroid accuracy. It can be noted that the attitude accuracy remains relatively unchanging, even under different background conditions and elevation angles. The attitude accuracy is, instead, limited by the few pixels that were used to sample the beacon in the centroid calculation. Figure 4-7 shows a map of the attitude accuracy as a function of beacon's true location on the detector for the minimum sky condition at

20° elevation. It can be seen that high attitude accuracy is achieved when the beacon location is close to the center of a pixel. On the other hand, the attitude accuracy degrades as the beacon location is near the edge of a pixel, with the worst case at the corner of a pixel, due to higher sensitivity to noise in the centroid calculation.
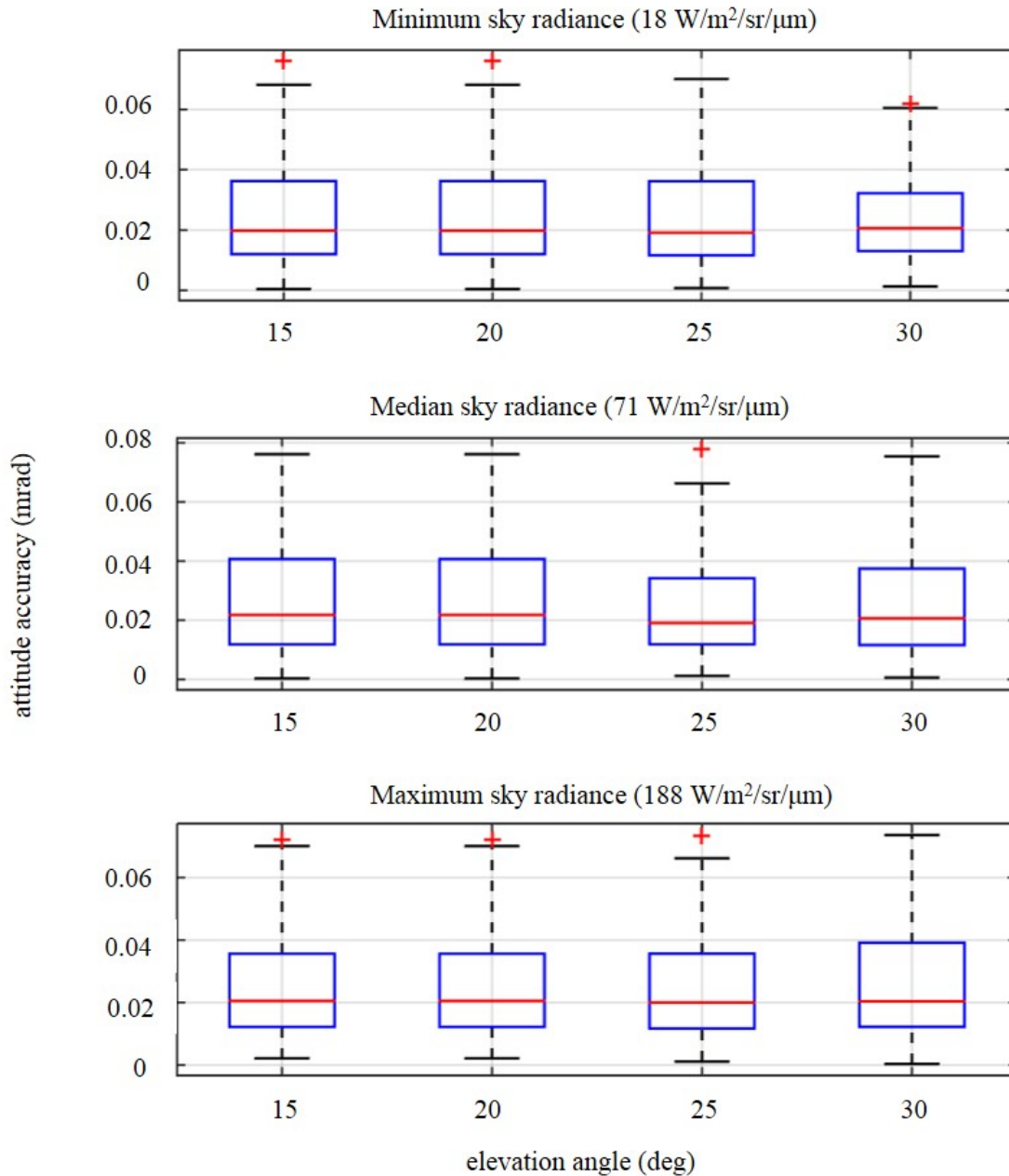
Figure 4-6: Attitude accuracy results from Monte-Carlo simulation for 3 representative sky conditions for elevation angles from 15° to 30°. In all cases, the attitude accuracy is less than 0.8 mrad.
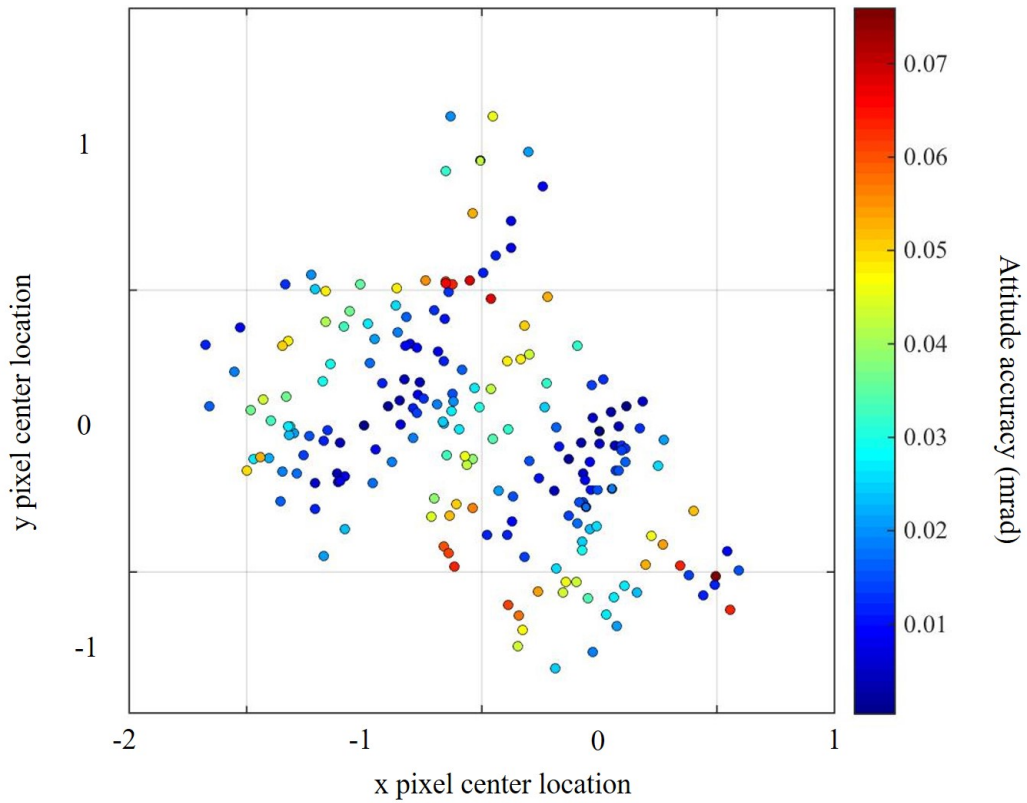
Figure 4-7: Attitude accuracy map as a function of the beacon's true location on the detector from Monte-Carlo simulation. Attitude accuracy, computed through COM centroid calculation, degrades as the beacon location is near the edge of a pixel.

Chapter 5

Conclusion

5.1   Summary

This thesis has detailed the development and analysis of a laser beacon tracking system for small satellites in low-Earth orbit to support a high-rate laser communication system. The motivation and background of this work was shown in Chapter 1, showing how laser beacon tracking system is necessary for laser communication, which holds the potential to relieve the small satellite communication bottle-neck. Chapter 2 describes the high-level laser communication architecture (NODE) and the beacon camera conceptual design and prototype development. The performance of the beacon camera is assessed through and end-to-end simulation development, as shown in Chapter 3, including both hardware and atmospheric channel models. The system's performance, quantified through fade probability and attitude accuracy, is presented in Chapter 4 for representative sky conditions and elevation angles.

The laser beacon camera presented in this work was designed to achieve high-accuracy attitude knowledge through acquisition of a laser beacon at 850 nm. The system was developed to support the NODE project, which aims to provide a laser downlink of 10-50 Mbps, achieved through pointing accuracy of better than $\pm 0.03°$ (0.5 mrad) relative to the ground station. The beacon system consists of a 5 MP CMOS detector and a 1" lens system with 35 mm focal length, providing an effective FOV of >6°, large enough to work with CubeSat coarse pointing capability. The bea-

con camera is equipped with a band-pass filter to improve the system's signal-to-noise ratio, and a long-pass filter to reduce ultraviolet damage to the system from sunlight. The beacon camera module's size and weight are equivalent to 0.1 U, consisting of only cost-efficient, COTS components.

The beacon tracking system performance was assessed through an end-to-end simulation, including four main models: link radiometry model, hardware model, atmospheric turbulence model, and Earth radiance model. The link radiometry model analysis was developed the compute the average optical power and the equivalent photon flux received by the camera's aperture. The hardware model determines the beacon image on the detector, following the lens' point-spread function and detector's resolution, along with other parameters such as quantum efficiency, optical losses, and noise figures. The atmospheric turbulence model was used to quantify the intensity fluctuation of the beacon due to inhomogeneity and turbulence in the atmosphere through modeling of the wind speed, refractive index profile, and scintillation index. Finally, Earth's upwelling radiance was computed through the use of on-orbit data from the LandSat-8 mission to provide the expected background noise level for a more accurate assessment of signal-to-noise ratio.

The simulation results provide the expected detection probability and attitude accuracy of the system under three representative sky spectral radiance scenarios. The detection probability was found through statistical estimation and Monte-Carlo simulation to be more than 90% for all sky conditions above 15° and more than 99% above 20° when there is no obstruction in the line-of-sight. Monte-Carlo simulations of the beacon image were utilized to find the expected attitude accuracy of the beacon camera. The simulation results show that the system can achieve an attitude accuracy of 0.2 mrad on average for all sky conditions above 15° when the beacon is found. The system's ability to locate the beacon is limited by the beacon image size on the detector relative to the pixel size, resulting in few pixel values used in the centroid calculation. In the worst case scenarios, the beacon system attitude error is still less than 0.1 mrad, equivalent to approximately $\frac{1}{10}$ of NODE's pointing budget, which was set at ± 1.05 mrad.

5.2   Contributions

The work presented in this thesis includes the development of one of the first high-accuracy ground-based CubeSat attitude sensing systems, capable of enabling high-rate laser communication on small-satellite platforms. In addition, atmospheric turbulence models and Earth's NIR brightness analysis were presented, showing the expected level of scintillation from a satellite in LEO and the range of Earth's upwelling spectral radiance at 850 nm. Lastly, the modular and reconfigurable beacon detection simulation provides system's performance assessment framework and guidelines for future ground laser beacon imaging efforts.

5.3   Future Work

The next steps in the development of the laser beacon tracking system include atmospheric model validation, hardware finalization and characterization, as well as more robust software development.

The atmospheric models used in the beacon simulation will be further validated with on-orbit data from previous missions. The atmospheric turbulence and background radiance model can be compared with OPALS' data from the beacon camera. Preliminary analysis has been done in comparing the OPALS beacon flux distribution with the estimated scintillation statistics. The results show that the simulated scintillation statistics agree with OPALS beacon flux distribution, with slightly higher scintillation index, possibly due to more conservative estimates in the atmospheric modeling process. More detailed analyses need to be done with considerations of important parameters such as elevation angles, sky conditions, and ground locations such that the atmospheric model can be properly validated.

Final hardware selection is necessary to ensure that the system can survive the launch and space environment. While the Edmund Optics lens system provides a low-cost lens system for lab-bench testing, it is not fabricated to be used in the space environment without modifications due to vacuum incompatible structural and

adhesive material. Future work will focus on the replacement of these materials or the use of alternative lens systems from Schneider Optics with space-heritage. Detailed descriptions of these lens systems are shown in Appendix A. The Matrix Vision camera module with Aptina detector has been on space missions as a star camera, according to the vendor. Further investigations will need to be carried out to ensure the camera is compatible with the launch and on-orbit environment.

Hardware characterization and testing will be carried out to validate hardware parameters specified by vendors and to assess the actual camera performance such that the simulation can be modified to correctly predict the performance on-orbit. Figure 5-1 shows an early lab-bench test setup effort to characterize the lens performance and detector's parameters. A 852-nm laser beam is expanded and collimated through a two-lens system before getting deflected by a mirror on a tip/tilt mount to control the field angle before entering the beacon camera system. The beacon image on the detector will be compared with expected results to characterize the beacon camera. A future test setup will consists of an interferometry system to confirm collimation, translation stages for easy adjustment at different field angles, and larger optics to overfill the camera aperture. After functionality and characterization, environmental testing will be done, including thermal vacuum and vibration testing.

Finally, more robust software development is capable of improving the detection probability and reducing the false-positive rate. Advanced image processing techniques can be used to recognize the beacon brightest pixel among other bright pixels, such as those caused by radiation damage and glints from reflective surfaces. During acquisition phase, multiple frames can be stacked to improve the signal-to-noise ratio without exceeding the well capacity causing saturation. In addition, a more detailed concept of operations will need to be established to handle unexpected loss of beacon due to cloud directly obstructing the line of sight or spacecraft disturbances.
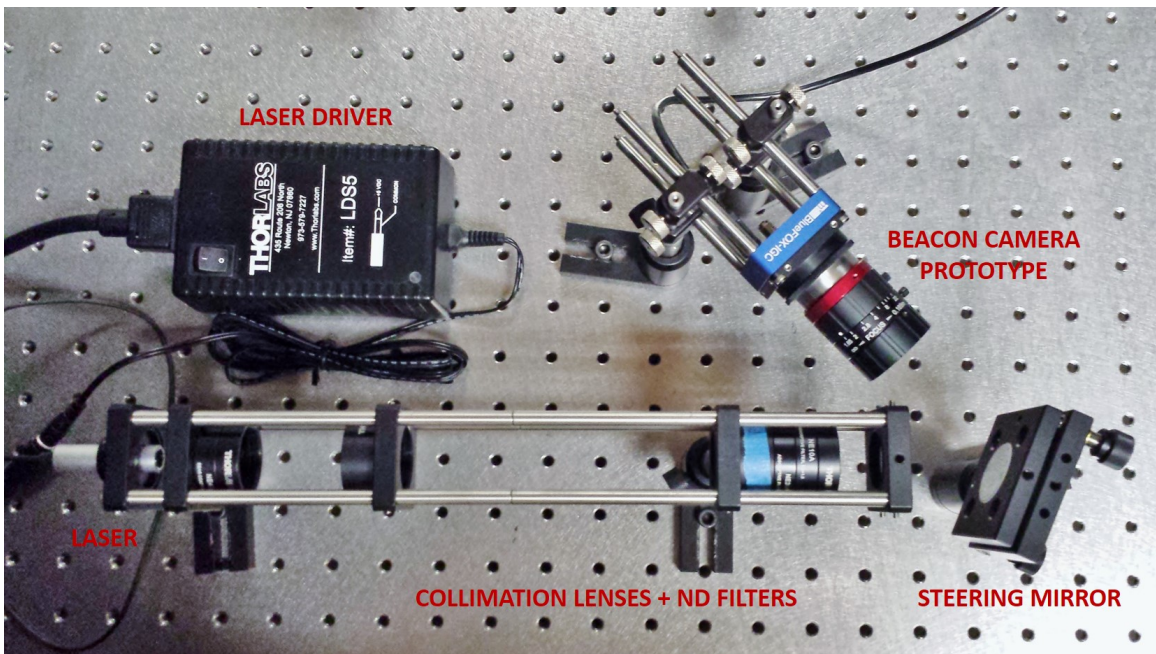
Figure 5-1: Lab-bench hardware characterization test setup, consisting of a 852-nm laser, collimating lenses, neutral density filters, steering mirror, and beacon camera

THIS PAGE INTENTIONALLY LEFT BLANK

Appendix A

Alternative Lens Systems

Schneider Optics
Xenoplan 1.9/35 mm Compact

Credit: Schneider Optics

Lens specifications	
F-number	1.9
Focal length	34.9 mm
Transmission	400-1000 nm
Interface	C-mount
Weight	92 g

Figure A-1: Schneider Optics Xenoplan lens system [43]

Schneider Optics
Apo-Xenoplan 1.8/35 mm

Credit: Schneider Optics

Lens specifications	
F-number	1.8
Focal length	35.2 mm
Transmission	400-1000 nm
Interface	C-mount
Weight	150 g

Figure A-2: Schneider Optics Apo-Xenoplan lens system [44]

THIS PAGE INTENTIONALLY LEFT BLANK

Bibliography

[1] H. Hemmati, *Near-Earth Laser Communications*. CRC Press - Taylor and Francis Group, 2009.

[2] A. Majumdar and J. Ricklin, *Free-Space Laser Communication*. Springer Science and Business Media LLC, 2008.

[3] S. Lambert and W. Casey, *Laser Communications in Space*. Artech House, Inc., 1995.

[4] NASA/IPAC. `http://www.ipac.caltech.edu/outreach/Edu/Windows/irwindows.html`. Accessed: 2015-08-19.

[5] D. Aviv, *Laser Space Communications*. Artech House, Inc., 2006.

[6] N. G. S. F. Center, "Nasa's lunar laser communication demonstration." `http://esc.gsfc.nasa.gov/267/271/335.html`. Accessed: 2015-08-19.

[7] E. Buchen and D. DePasquale, "2014 nano / microsatellite market assessment." Spaceworks Enterprises, Inc. (SEI), Atlanta, GA, 2014.

[8] M. Swartwout, "The first one hundred cubesats: A statistical look," *Journal of Small Satellites, Vol. 2, No.2, pp. 213-233*, 2013.

[9] "Cubesat design specification(cds)rev 13." The CubeSat Program, Cal Poly SLO, 2014.

[10] CubeSat Kit, "3D CAD Design." `http://www.cubesatkit.com/content/design.html`. Accessed: 2015-08-19.

[11] J. Hanson, J. Chartres, H. Sanchez, and K. Oyadomari, "The EDSN intersatellite communications architecture," *28th Annual AIAA/USU Conference on Small Satellites*, 2014.

[12] K. Sarda, C. Grant, M. Chaumon, S. Y. Choi, B. Johnston-Lemke, and R. Zee, "On-orbit performance of the bright target explorer (BRITE) nanosatellite astronomy constellation," *28th Annual AIAA/USU Conference on Small Satellites*, 2014.

[13] W. Marshall and C. Boshuizen, "Planet labs' remote sensing satellite system," in *CubeSat Developers' Workshop 2013*, 2013.

[14] B. Klofas, "Survey of cubesat communication systems: 2009-2012," in *Presented at the 10th Annual CubeSat Developers' Workshop, San Luis Obispo, California*, 2013.

[15] S. Palo, G. Stafford, and A. Hoskins, "An agile multi-use nano star camera for constellation applications," *27th Annual AIAA/USU Conference on Small Satellites*, 2013.

[16] E. Kahr, O. Montenbruck, and K. O'Keefe, "Estimation and analysis of two-line elements for small satellites," *Journal of Spacecraft and Rockets, Vol. 50, No. 2*, 2013.

[17] D. Boroson, B. Robinson, D. Burianek, D. Murphy, and A. Biswas, "Overview and status of the lunar laser communication demonstration," *Proc. SPIE 8246, Free-Space Laser Communication Technologies XXIV*, 2012.

[18] M. Abrahamson, B. Oaida, O. Sindiy, and A. Biswas, "Achieving operational two-way laser acquisition for OPALS payload on the international space station," *Proc. SPIE 9354, Free-Space Laser Communication and Atmospheric Propagation XXVII*, 2015.

[19] S. Janson and R. Welle, "The NASA optical communication and sensor demonstration program: An update," *28th Annual AIAA/USU Conference on Small Satellites*, 2014.

[20] J. Burnside, S. Conrad, A. Pillsbury, and C. DeVoe, "Design of an inertially stabilized telescope for the LLCD," *Proc. SPIE 7923, Free-Space Laser Communication Technologies XXIII*, 2011.

[21] B. Oaida, M. Abrahamson, R. Witoff, J. Martinez, and D. Zayas, "OPALS: An optical communications technology demonstration from the international space station," *Aerospace Conference, 2013 IEEE*, 2013.

[22] S. Janson and R. Welle, "The NASA optical communication and sensor demonstration program," *27th Annual AIAA/USU Conference on Small Satellites*, 2013.

[23] T. Nguyen, K. Riesing, R. Kingsbury, and K. Cahoy, "Development of a pointing, acquisition, and tracking system for a cubesat optical communication module," *SPIE 9354, Free-Space Laser Communication and Atmospheric Propagation XXVII*, 2015.

[24] R. Kingsbury, D. Caplan, and K. Cahoy, "Compact optical transmitters for cubesat free-space optical communications," *Proc. SPIE 9354, Free-Space Laser Communication and Atmospheric Propagation XXVII*, 2015.

[25] A. Schwarzenberg-Czerny *et al.*, "The BRITE nano-satellite constellation mission," *38th COSPAR Scientific Assembly. Held 18-15 July 2010, in Bremen, Germany, p.15*, 2010.

[26] J. Gangestad, B. Hardy, and D. Hinkley, "Operations, orbit determination, and formation control of the AeroCube-4 CubeSats," *Proc. of 27th AIAA/USU Conference on Small Satellites*, 2013.

[27] R. Kingsbury, K. Riesing, and K. Cahoy, "Design of a free-space optical communication module for small satellites," *Proc. of 28th AIAA/USU Conference on Small Satellites*, 2014.

[28] R. Kingsbury, T. Nguyen, K. Riesing, and K. Cahoy, "Fast-steering solutions for cubesat-scale optical communication," *Proc. of International Conference on Space Optics*, 2014.

[29] B. Oaida *et al.*, "Optical link design and validation testing of the optical payload for lasercomm science (OPALS) system," *Proc. SPIE 8971, Free-Space Laser Communication and Atmospheric Propagation XXVI*, 2014.

[30] U.S. Department of Transportation Federal Aviation Administration, "Advisory circular - outdoor laser operations," 2004.

[31] P. Magnan, "Detection of visible photons in CCD and CMOS: A comparative view," *Proceedings of the 3rd International Conference on New Developments in Photodetection*, 2003.

[32] Aptina Imaging, "1/2.5-inch 5mp cmos digital image sensor mt9p031 data sheet, rev. g."

[33] Fairchild Imaging, "Fairchild Imaging CIS2521F 5.5 Megapixel CMOS Image Sensor."

[34] Edmund Optics, "35mm VIS-NIR Compact Fixed Focal Length Lens." `http://www.edmundoptics.com/imaging-lenses/fixed-focal-length-lenses/compact-vis-nir-fixed-focal-length-lenses/67716/`. Accessed: 2015-08-19.

[35] Edmund Optics, "850nm CWL, 10nm FWHM, 25mm Mounted Diameter." `http://www.edmundoptics.com/optics/optical-filters/bandpass-filters/traditional-coated-700-999nm-bandpass-interference-filters/67852/`. Accessed: 2015-08-19.

[36] Edmund Optics, "M25.5 x 0.5 Mounted UV/VIS Cut-off Filter (R-72)." `http://www.edmundoptics.com/optics/optical-filters/longpass-edge-filters/mounted-infrared-ir-filters/65796/`. Accessed: 2015-08-19.

[37] J. Strohbehn, *Laser Beam Propagation in the Atmosphere*. Springer-Varlag Berlin Heidelberg, 1978.

[38] L. Andrews and R. Phillips, *Laser Beam Propagation through Random Media, Second Edition*. SPIE Press Monograph Vol. PM152, 2005.

[39] D. Roy *et al.*, "Landsat-8: Science and product vision for terrestrial global change research," *Remote Sensing of Environment Volume 145, pp. 154 - 172*, 2014.

[40] U.S. Geological Survey (USGS), "Earth resources observation and science (EROS) LandSat 8 OLI/TIRS database." `http://earthexplorer.usgs.gov`.

[41] D. Roy *et al.*, "Summary of current radiometric calibration coefficients for Landsat MSS, TM, ETM+, and EO-1 ALI sensors," *Remote Sensing of Environment Volume 113, pp. 893 - 903*, 2009.

[42] NASA Goddard Space Flight Center, "Landsat 7 science data users handbook." `http://landsathandbook.gsfc.nasa.gov/pdfs/Landsat7_Handbook.pdf`. Accessed: 2015-08-19.

[43] Schneider Optics, "Xenoplan 1.9/35mm compact." `https://www.schneideroptics.com/Ecommerce/CatalogItemDetail.aspx?CID=1377&IID=5967`. Accessed: 2015-08-19.

[44] Schneider Optics, "Apo-xenoplan 1.8/35mm compact." `https://www.schneideroptics.com/Ecommerce/CatalogItemDetail.aspx?CID=1547&IID=7051`. Accessed: 2015-08-19.